

Direct observation of phase change accommodating hydrogen uptake in bimetallic nanoparticles

Lívia P. Matte,¹ Maximilian Jaugstetter,² Tara P. Mishra,³ Carlos Escudero,⁴ Giuseppina Conti,^{5,6} Slavomir Nemsak,^{5,6*} Fabiano Bernardi^{1*}

¹ Programa de Pós-Graduação em Física, Instituto de Física, Universidade Federal do Rio Grande do Sul (UFRGS), Porto Alegre, RS, 91501-970, Brazil

² Chemical Sciences Division, Lawrence Berkeley National Laboratory, Berkeley, CA, 94720, USA

³ Materials Science Division, Lawrence Berkeley National Laboratory, Berkeley, CA, 94720, USA

⁴ ALBA Synchrotron Light Source, Cerdanyola del Vallès, Barcelona, 08290, Spain

⁵ Advanced Light Source, Lawrence Berkeley National Laboratory, Berkeley, CA, 94720, USA

⁶ Department of Physics and Astronomy, University of California, Davis, CA, 95616, USA

* e-mail: SNemsak@lbl.gov; bernardi@if.ufrgs.br;

Abstract

Hydrogen is a promising alternative to fossil fuel, however storing it efficiently poses challenges. One promising solution is to adsorb hydrogen on solid materials demonstrating quasi-molecular bonding with hydrogen. The hydrogen adsorption energy can be tuned by changing the morphology or stoichiometry of bimetallic nanoparticles. Here we used complementary techniques to unveil the chemical compositional and morphological transformation undergone by Pd_xNi_{100-x} nanoparticles during H₂ adsorption. Our findings reveal NiO-rich shell and Pd-rich core as confirmed by X-ray photoelectron spectroscopy, X-ray scattering, and electron energy loss spectroscopy. During hydrogen adsorption, which mainly occurs on Pd atoms, the Pd-rich core fragments into small pockets, increasing its surface area. This process is more pronounced for nanoparticles with lower Pd loading, emphasizing the role of NiO. These results shed light on the atomic changes occurring in the

Pd_xNi_{100-x} nanoparticles during hydrogen adsorption and can be applicable on multi-metallic systems to improve hydrogen storage properties.

Keywords: hydrogen storage, morphology changes, bimetallic nanoparticles, in situ measurements, core-shell structure.

1. Introduction

The use of non-renewable energy sources is directly related to climate change due to the emission of greenhouse gases. It is estimated that natural gas and oil reserves will be depleted before 2070,¹ creating energy insecurity in economies based on these fuels. Thus, it is urgent to dramatically change the world's energy matrix to a more renewable and sustainable one. Hydrogen is the most promising candidate to replace fossil fuels since it is available from renewable energy sources.² It presents a gravimetric density 3 times bigger than gasoline, for example.² Another benefit is that byproducts of energy generation using hydrogen consist mainly of H₂O. However, the main challenge for the large-scale use of hydrogen as an energy carrier in light-duty vehicles is the hydrogen storage process. The currently available methods make it commercially disadvantageous. Hence, the US Department of Energy (DOE) set audacious targets for hydrogen storage materials that should be fulfilled by 2025, but we are still far away from reaching it.³

A promising way to store hydrogen is using solid materials,⁴ where the hydrogen can be either adsorbed at the surface or stored with the formation of a hydride phase. For instance, hydrogen can be adsorbed on the activated carbon surface, which has a high gravimetric capacity, but presents a very low volumetric capacity.⁴ On the other hand, complex metal hydrides, such as LiAlH₄, present a high gravimetric and volumetric capacity, but too high desorption temperatures.⁴ Thus, the discovery of improved storage materials is still needed before a full-scale commercialization can be realized.

The material used to adsorb hydrogen should present an adsorption energy in the quasi-molecular bonding regime, between roughly 0.2 eV and 0.6 eV.⁵ The major candidates are metallic nanostructures, where the adsorption energy can be adjusted by their morphology.²

Pd is known to have a high affinity with hydrogen and to form a stable Pd-H bond.⁶ However, the current Pd nanostructures do not get even close to fulfilling the DOE targets.⁶ Nevertheless, the adsorption energy may be adjusted also through the stoichiometry in bimetallic nanoparticles.⁴ Switching from monometallic to bimetallic nanostructures allows the creation of new atomic sites for hydrogen adsorption, thus improving the hydrogen storage capacity.⁷ It is well known that NiO presents a lower affinity with hydrogen than Pd, although it was demonstrated by our group⁸ that NiO nanofoams present a quasi-molecular bonding with hydrogen. Therefore, a mixture of NiO to Pd in the form of Pd-NiO nanoparticles shows great promise for hydrogen storage applications. The inclusion of NiO is helpful also to reduce the cost compared to monometallic Pd. Previous studies demonstrated that the bimetallic Pd-Ni nanoparticles are great candidates for promoting efficient hydrogen storage.⁹⁻¹¹ Thus, it is fundamental to thoroughly understand the atomic events occurring during hydrogen adsorption in these bimetallic nanoparticles in order to design improved hydrogen storage systems.

We herein present an approach utilizing complementary *in-situ* techniques to determine atomic- and nano-scale transformations during the hydrogen storage process in Pd_xNi_{100-x} (x = 90, 75, 50, and 25) nanoparticles. Each technique is dedicated to probing different chemical and structural properties of the nanoparticles during the process. X-ray absorption spectroscopy (XAS) was used to observe the changes in the local atomic order around Ni and Pd atoms, X-ray photoelectron spectroscopy (XPS) probes the chemistry of components, and grazing incident X-ray scattering (GIXS) observed structural transformations. Measurements are complemented by the transmission electron microscopy (TEM) combined with electron energy loss spectroscopy (EELS) for nano-scale insights into particles' morphology and chemistry. The combination of all techniques reveals complex atomic mechanisms promoting the hydrogen storage in these bimetallic nanoparticles.

2. Results and discussion

Initial *ex-situ* characterization of morphology and composition of nanoparticles was performed by scanning transmission electron microscopy - high-angle annular dark field (STEM-HAADF) imaging. Figure 1(a) presents a typical image obtained for Pd₂₅Ni₇₅ nanoparticles, showing a nanoparticle with a diameter of around 20 nm. The histogram of

size distribution from TEM images shows similar size for all compositions (Figure S1). Figure 1(b) presents the XRD measurements, the indexing with the crystal phases, and the Rietveld refinement. The presence of NiO and PdO phases is observed in all samples, besides the Pd(0) phase in smaller amounts in the Pd-richer samples, which agrees with XANES measurements in Figure S2. In general, NiO and PdO phases have almost the same crystallite size for all the samples (Table S1). The XRD and TEM results show that the bimetallic nanoparticles exhibit almost the same diameter, morphology, and oxidation state. Moreover, the Pd content obtained from surface-sensitive XPS measurements in the as-prepared state is always smaller than that obtained from EDS measurements (Figure S3), indicating that all as-prepared samples present a core-shell-like structure with a Ni-rich shell and a Pd-rich core region. In addition, EDS maps show that Ni and Pd are well dispersed in the samples (Figure S4).

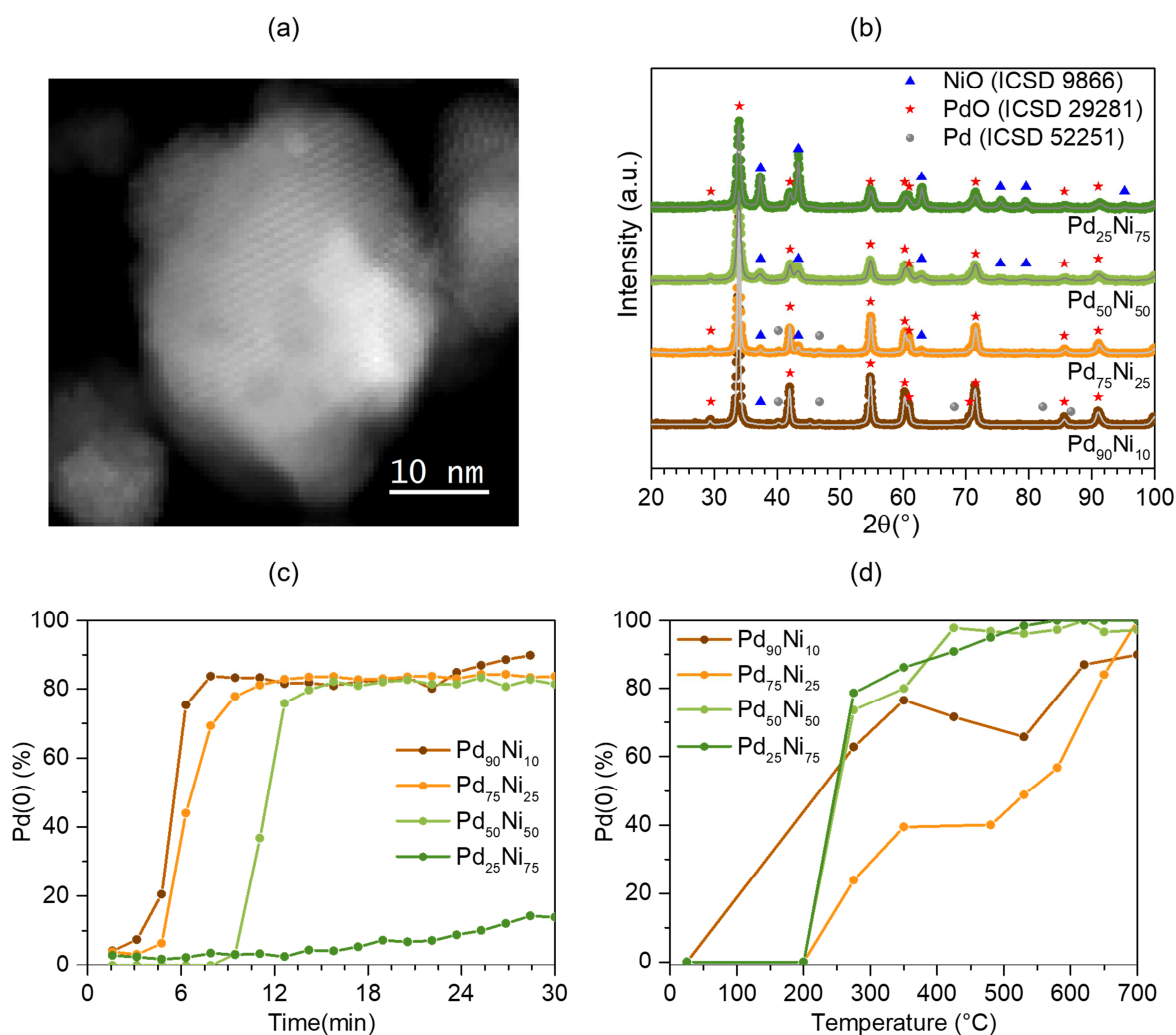


Figure 1: (a) Typical HAADF-STEM image of the $Pd_{25}Ni_{75}$ sample. (b) XRD measurements of the Pd_xNi_{100-x} samples. The points represent the experimental data, and the gray line represents the fit obtained from the Rietveld refinement. The blue triangle, red star, and gray circle show the position of the Bragg reflections related to the NiO, PdO, and Pd(0) crystalline phases, respectively. (c) Pd(0) fraction as a function of time obtained from *in-situ* XANES measurements during the 30 mL/min 4% H_2 + 96% He exposure at room temperature and (d) on the nanoparticles' surface obtained from the XPS measurements under UHV as a function of temperature.

The reduction of Pd atoms is an essential step in the hydrogen storage process since Pd(0) has a much higher hydrogen storage capacity than PdO.¹² The opposite occurs with Ni atoms, where NiO presents adsorption energy in the quasi-molecular bonding regime, while Ni(0) presents adsorption energy in the chemisorption regime.⁸ Figure 1(c) shows the Pd(0) content obtained from the *in-situ* XANES analysis as a function of time during the hydrogen exposure at RT (Figure S5). The initial high amount of PdO quickly reduces to Pd(0), as expected.^{13,14} Moreover, the time needed to reduce nanoparticles from PdO to Pd(0) strongly depends on the Pd/Ni ratio. The higher the amount of Pd, the faster the Pd reduction at RT under H_2 exposure, suggesting that Ni plays an important role in the reduction process of Pd. This can be related to the existing core-shell-like structure. The Ni-richer samples present a thicker shell, acting like a diffusion barrier for the H_2 molecules. In addition, NiO is not reduced to Ni(0) under these conditions, as illustrated by *in-situ* XANES measurements at Ni K edge (Figure S6), in agreement with previous reports.¹⁵

The near-surface region of the as-prepared samples exhibits only NiO and PdO chemical components, as observed by XPS (Figure S7). The atomic content of reduced Pd(0) as a function of temperature, obtained from the analysis of the AP-XPS spectra (Figure S8) measured under ultra-high vacuum (UHV), is shown in Figure 1(d). It is observed that the total surface reduction occurs at higher temperatures for samples containing higher amounts of Pd. Since the thermally-induced reduction process does not depend on the diffusion of H_2 molecules through the NiO layer, this behavior follows the opposite trend from the RT reduction in the H_2 gas environment.

Aiming to observe the changes in the local atomic order around Ni and Pd atoms during the hydrogen adsorption process, *in-situ* EXAFS measurements were performed. Figure 2 shows the Fourier Transform (FT) of the EXAFS oscillations (shown in Figure S9 and S10) for nanoparticles with different Pd/Ni ratios during H_2 exposure at RT and atmospheric pressure. The FT data of all the samples are very similar to Pd(0) and NiO standards. However, the

$\text{Pd}_{25}\text{Ni}_{75}$ sample also shows a small contribution from the Pd-O scattering path along with the Pd(0). Surprisingly, there is a clear decrease in the intensity of the peak related to the Pd-Pd scattering path in the nanoparticles in comparison to Pd(0) standard, but the same does not occur for Ni-O and Ni-Ni paths. This is related to a reduced size or higher temperature of the sample. Since all measurements were conducted at RT, it shows some atomic rearrangement around Pd atoms different than Ni atoms. Under H_2 exposure, the Pd-Pd scattering peak shifts to higher R values as compared to the Pd(0) standard, indicating lattice expansion upon H_2 uptake. Furthermore, no shifts in the Ni-Ni or Ni-O scattering paths are observed compared to NiO standard during H_2 exposure.

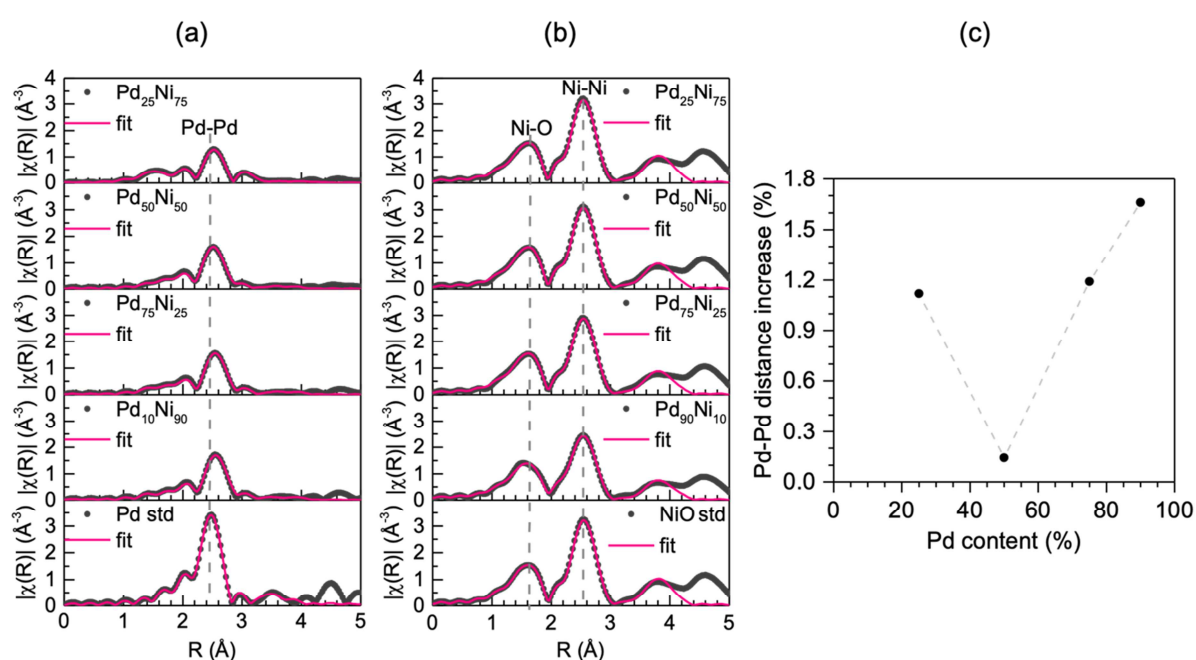


Figure 2: Fourier Transform of the EXAFS oscillations at the (a) Pd K edge and (b) Ni K edge during H_2 exposure at RT and atmospheric pressure. The black dots represent the data measured and the pink line the fit performed. (c) Increase of the Pd-Pd atomic distance in comparison to Pd standard position as a function of Pd content in the nanoparticles.

Figure 2(c) displays the relative increase in the Pd-Pd scattering path distance from the coordination shell when compared to the Pd(0) reference (see Table S2 for the fitting parameters). There is an increasing trend of the Pd-Pd interatomic distance (up to 1.7% increase) with the Pd amount, with the exception of $\text{Pd}_{50}\text{Ni}_{50}$ nanoparticles that present only a slight increase. From the d-band theory,¹⁶ it is known that the strain influences the hydrogen adsorption properties. Lattice expansion upshifts the d-band center, leading to a stronger

adsorbate binding. The increase in the Pd-Pd interatomic distance may also be related to the absorption of hydrogen in the interstitial sites around Pd atoms, thus increasing the lattice size, as observed in the literature.^{17,18} Therefore, due to the highest increase in the R value and the highest Pd content of studied stoichiometries, it is expected that Pd₉₀Ni₁₀ sample would have the highest hydrogen adsorption capacity. In corollary, although Pd₇₅Ni₂₅ and Pd₂₅Ni₇₅ present a similar increase in the R value, the former is expected to exhibit a higher hydrogen adsorption capacity due to the higher Pd content. Since no shifts are observed in the Ni-Ni or Ni-O scattering peaks (Table S3), it indicates that hydrogen is adsorbed mainly in the Pd interstitial sites.

In order to observe the initial stages of the hydrogen adsorption process starting at the surface of the nanoparticles, AP-XPS measurements were performed. The initial heat treatment at 250 °C under UHV facilitates organic remnants removal and the reduction of PdO to Pd(0), as demonstrated in Figure 1(d). After the annealing treatment, the samples were exposed to 100 mTorr H₂ while AP-XPS measurements were performed. Figure 3 (a) and (b) show typical Pd 3d and Ni 3p AP-XPS measurements for the Pd₂₅Ni₇₅ nanoparticles using incident beam photon energies of 695 eV and 1000 eV, respectively. Different photon energies allow probing different depths in the nanoparticles since the inelastic mean free path (λ) of photoelectrons coming from the Pd 3d electronic region is around 13 Å (1000 eV) or 8 Å (695 eV). The spectra for all other bimetallic samples are shown in Figure S11 and S12. The measurements were carried out at RT, before and during exposure to 100 mTorr of H₂. The peak at around 336 eV (Figure 3 (a)) is assigned to the Pd(0) component.¹⁹ For Pd₉₀Ni₁₀ nanoparticles, it is observed that the nanoparticles are not fully reduced after thermal treatment since they show a shoulder at higher binding energies (around 338 eV), which is associated with PdO (see Figure S11 (a)).¹² This shoulder disappears when the sample is exposed to H₂, thus showing the full reduction of PdO to Pd(0). The small binding energy shifts in Pd 3d and Ni 3p regions are discussed in more detail in Note S1. It is important to note that the absolute binding energy values and shifts for suspended nanoparticles are not always indicative of a chemical change. The electrostatic alignment between the particle and substrate can result in apparent shifts,²⁰ as it is believed to be the case here as well. The presence of a doublet at around 349 eV is also observed, which is attributed to the Ca 2p core level that comes from the synthesis procedure. The main component at the Ni 3p AP-XPS region (Figure 3(a)) at around 70 eV comes from NiO.²¹ In this energy region, the peak at around 65 eV is associated with Na 2s electronic region, which similarly to Ca, is a

contaminant coming from the synthesis and transfer of nanoparticles. However, no contamination was observed by EDS in these samples (see Figure S13), showing that this contamination may be in small amounts on the surface of the nanoparticles.

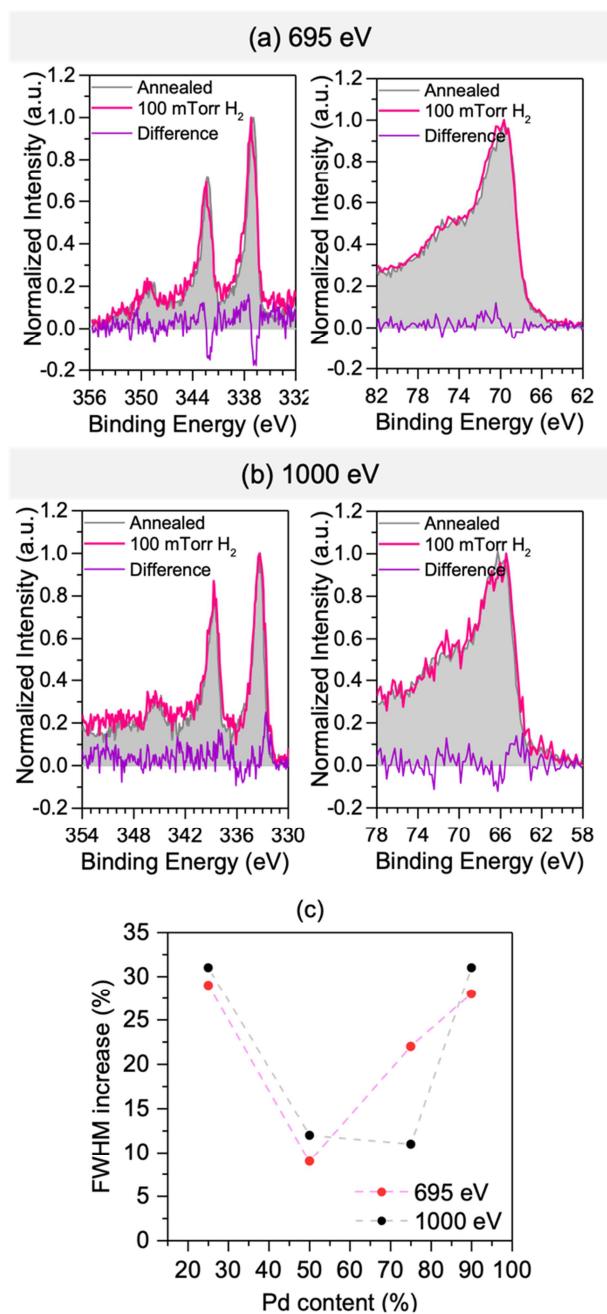


Figure 3: Typical AP-XPS measurements of the $Pd_{25}Ni_{75}$ nanoparticles in the Pd 3d and Ni 3p energy regions using a photon energy of (a) 695 eV and (b) 1000 eV. The grey and pink lines represent the measurement after annealing under UHV and during 100 mTorr H_2 exposure for 2h at RT, respectively. The difference between the spectrum during the H_2 exposure process and the spectrum measured after annealing is presented below each spectra in purple. (c) Relative increase in the FWHM of the peak related to Pd(0) when comparing the Pd 3d spectra after annealing and during H_2 exposure, as a function of Pd content in the nanoparticles.

The introduction of H₂ atmosphere induces an increase in the FWHM value of the Pd(0) component. The widening starts to occur at H₂ pressures as low as 1x10⁻⁷ Torr but stabilizes at 100 mTorr, as shown in Figure S14. Figure 3(c) displays the relative increase in the FWHM value of the Pd(0) component during H₂ exposure in comparison to the value before the insertion of H₂ atmosphere obtained from the fitting procedure shown in Figure S15 (see Table S4). All the samples present a clear increase in the FWHM value in this period for both photon energies used. This is indicative of the presence of a second Pd component related to the Pd-H bonding. However, due to the binding energy proximity of Pd(0) and Pd-H components, which is around 0.2 eV,²² it is not possible to distinguish the two components in the AP-XPS measurements. In almost all the samples, this increase in the FWHM value is more significant for the measurements performed using an incident beam of 1000 eV than 695 eV. The more significant increase in the FWHM value for the higher excitation energy of 1000 eV indicates the presence of more Pd-H bonds in the subsurface layers. In general, higher the amount of Pd in the composition, higher the relative increase in the FWHM value. However, Pd₂₅Ni₇₅ sample also presents a high relative increase due to the relatively low amount of Pd atoms that can readily form Pd-H bonds.

On the other hand, Ni 3p AP-XPS region typically shows no changes in intensity or shape due to H₂ exposure, thus indicating the preferential bonding of hydrogen with Pd atoms, in agreement with *in-situ* XAS results. However, for the highest Ni amount sample (Figure 3 (a,b)), a small increase in the FWHM of the Ni 3p region is also observed. This may indicate that hydrogen starts to be co-adsorbed on Ni atoms in the close proximity of Pd, which readily forms Pd-H bonds. However, this is hard to detect through the *in-situ* XAS measurements presented because they are bulk-sensitive.

Since hydrogen adsorption occurs predominantly on the Pd atoms, it is essential to evaluate how the Pd/Ni ratio at the surface changes during the hydrogen adsorption process. Thus, the Pd atomic fraction at the sample surface was calculated by normalizing the Pd 4p and Ni 3p areas by their respective photoionization cross-sections.²³ Inelastic mean free path of these core-electrons was around 15 Å (1000 eV) and 11 Å (695 eV). Figure S3 shows that in all cases, Pd content at the surface is significantly smaller than that obtained by EDS. As explained above, it indicates the presence of a core-shell-like structure with a Ni-rich shell and a Pd-rich core region, even during the H₂ exposure. For the metallic Pd-Ni system, the opposite is theoretically expected, *i.e.*, a Pd-rich shell and a Ni-rich core,²⁴ but the Ni-rich

surface comes due to the stability of NiO . Also, there is a slight increase in the Pd content at the surface region during hydrogen exposure, showing a change in the atomic arrangement of the nanoparticles.

AP-GIXS measurements were performed to gain a further understanding of the atomic rearrangement taking place in the nanoparticles during the treatment. Figure 4(a) presents a typical AP-GIXS measurement for the as-prepared Pd₂₅Ni₇₅ sample. To minimize the influence of the silica substrate, data analysis was performed on a horizontal line-cut as indicated by the red line in Figure 4(a).²⁵ Figure 4(b) presents the pair distance distribution function (PDDF) obtained from the inverse Fourier transform of the line-cut. A decrease in the maximum R value, which defines the maximum distance between two scattering atoms in a single nanoparticle, is observed after the annealing process. Similarly, there is a clear decrease in the Radius of Gyration (Figure 4(c)), which is a shape-independent indicator of particle size,^{26,27} with the treatment employed, mainly after heating to 250 °C. These results indicate the contraction of the Pd₂₅Ni₇₅ nanoparticles after the annealing process. This contraction can be attributed to the reduction of PdO to Pd(0).

Figure 4 (d-f) presents the electron density reconstruction of the PDDF of the Pd₂₅Ni₇₅ nanoparticles under the different treatments applied (see Note S2).²⁸ Pd(0) has the highest electron density of all compounds in the nanoparticles, while NiO has the lowest electron density value (Table S5). Figure 4(d) shows that the as-prepared Pd₂₅Ni₇₅ nanoparticles have an ellipsoid shape of ~30 nm length and ~20 nm width, which is in good agreement with the obtained AFM images of these particles (see Figure S16) and conducted GIXS simulations (see Figure S17). The particles have high electron density in the core region, while a lower density is observed in the shell region, indicating the presence of a Pd-rich core and Ni-rich shell. The size and shape of as-prepared nanoparticles are confirmed by HAADF-STEM (Figure 1(a)). Figure 4(e) presents the PDDF reconstruction of the Pd₂₅Ni₇₅ nanoparticles after annealing in UHV. A shape change from an ellipsoid-like to a spherical-like particle is clearly observed. Again, a higher electron density is present in the core region of these nanoparticles as compared to the shell. However, this high-density core is more diffuse in comparison to the as-prepared case. Lastly, the Pd₂₅Ni₇₅ nanoparticles during exposure to 100 mTorr H₂ retain their spherical shape (Figure 4(f)). Surprisingly, the inner structure of the nanoparticle undergoes a transformation, in which segmentation of high-electron density pockets inside the nanoparticle and their diffusion towards the surface is observed. This

segregation is induced by the adsorption of hydrogen mainly onto the Pd atoms, as confirmed by *in-situ* XAS and AP-XPS measurements. Interchange of atoms in a core-shell structure under a reducing or oxidizing atmosphere has been widely observed for many different bimetallic systems at elevated temperatures.²⁹ However, the interchange of atoms from the Pd core into the nanoparticle shell at RT, as observed here, causes the core to split into Pd pockets inside a Ni shell. In addition, a formation of well-defined high-density structures is observed. To the best of our knowledge, this is the first time the segregation of the core of the nanoparticle into small pockets has been observed *in-situ* induced by exposure to hydrogen at room temperature.

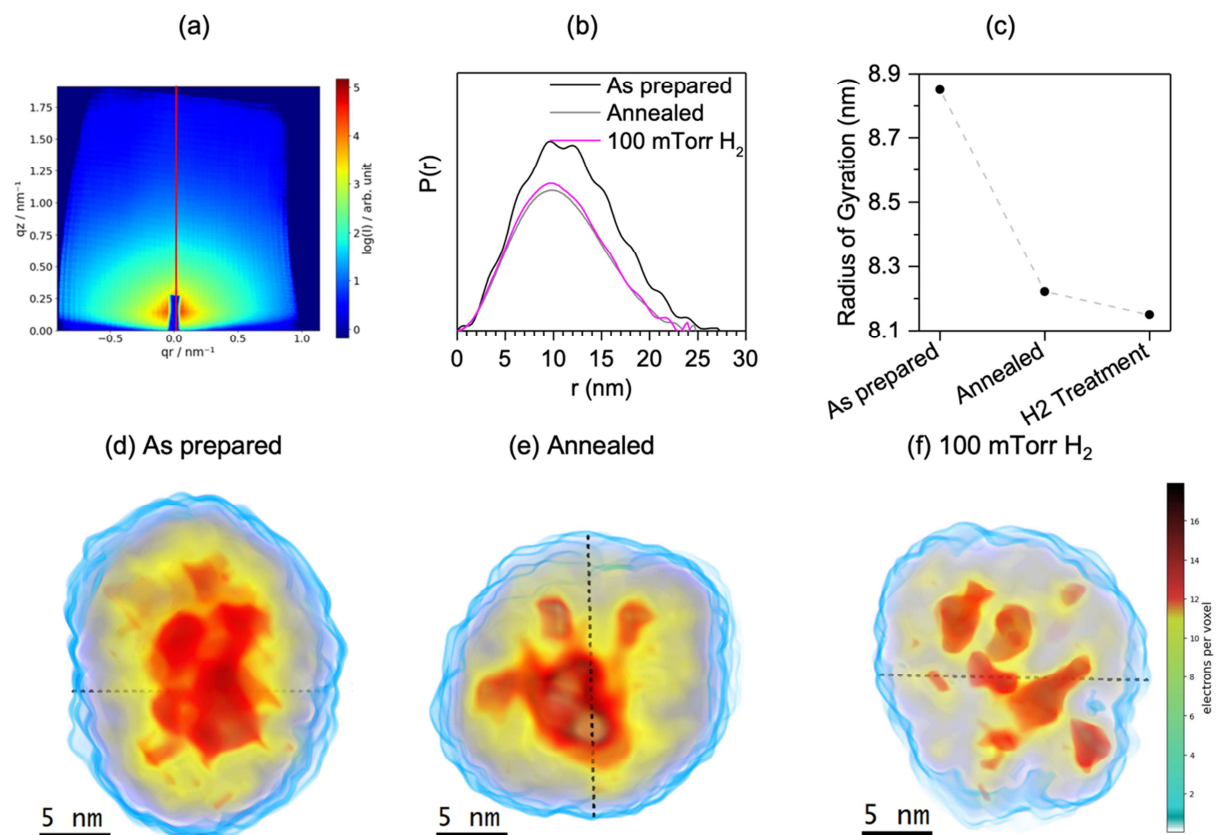


Figure 4: (a) Typical AP-GIXS measurement of the as-prepared $Pd_{25}Ni_{75}$ nanoparticles. The red straight line represents the position of the cut used in the analysis. (b) Pair distance distribution function (PDDF) obtained from the inverse Fourier transform of the cut presented in (a) for the $Pd_{25}Ni_{75}$ as prepared, annealed, and under 100 mTorr H_2 atmosphere, presented in black, red, and green, respectively. (c) Radius of gyration as a function of the treatment applied. On the bottom, reconstruction of the electronic density inside the $Pd_{25}Ni_{75}$ nanoparticles for the (d) as prepared, (e) annealed, and (f) under 100 mTorr H_2 atmosphere. In red is presented the region with higher electronic density, yellow, medium electronic density, and blue, lower electronic density.

The same analysis procedure was applied to the other $\text{Pd}_x\text{Ni}_{100-x}$ compositions, as shown in Figure 5(a-c) for 100 mTorr H_2 exposure. The same qualitative behavior is observed for all three stoichiometries (see Figure S18 for the annealed sample), *i.e.*, the core region with a higher electron density in comparison to the shell region and the formation of fragmented high electronic density pockets. It explains the small intensity at FT for Pd K edge and the same intensity for Ni K edge in comparison to Pd(0) and NiO standards (Figure 2).

Figure 5(d) shows the relative expansion of the nanoparticles during the exposure to 100 mTorr H_2 in comparison to before H_2 introduction as a function of Pd content. A contraction of the $\text{Pd}_{25}\text{Ni}_{75}$ and $\text{Pd}_{50}\text{Ni}_{50}$ nanoparticles is observed, while the $\text{Pd}_{75}\text{Ni}_{25}$ nanoparticles undergo an expansion during H_2 exposure. The expansion is related to the increase in the Pd lattice size when hydrogen is adsorbed in the interstitial site, as determined by *in-situ* XAS measurements. However, due to the low amount of Pd and the complicated rearrangement of the Pd pockets inside the nanoparticles, $\text{Pd}_{25}\text{Ni}_{75}$ and $\text{Pd}_{50}\text{Ni}_{50}$ nanoparticles exhibit a size contraction.

Moreover, Figure 5(e) shows the relative expansion of the sphere enclosing all the high-electron density pockets as a function of the Pd content in the sample. Such analysis utilizing an equivalent sphere is typically used for fractal nanoparticle systems to compare different shape configurations.³⁰ For lower Pd concentrations, a pocket enclosure expansion of 20% is observed. This occurs by the dissolution of high electron density regions inside the nanoparticles with lower Pd content. A contraction occurs for the nanoparticles containing a higher Pd concentration. Figure 5(f) shows the increase in the FWHM of the electronic density distribution curve across the particle, as shown in Figure S19.

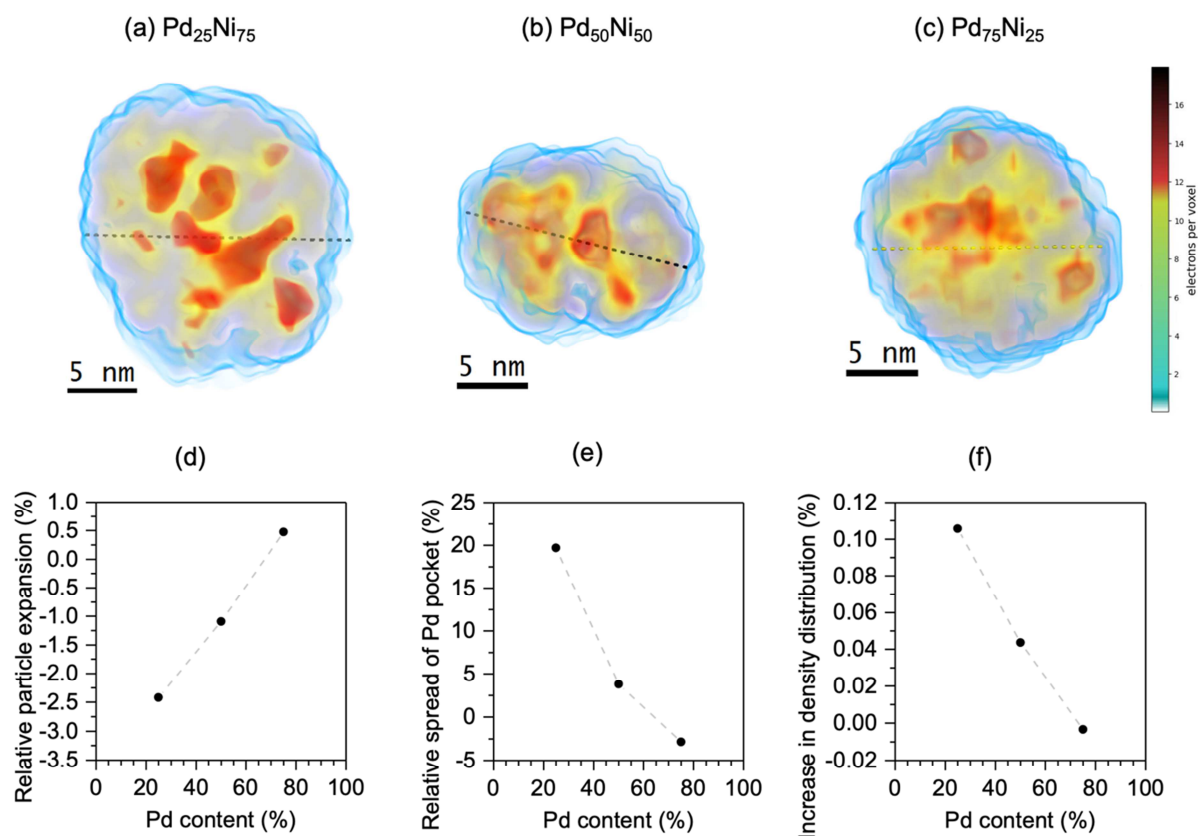


Figure 5: Reconstruction of the electronic density under 100 mTorr H_2 atmosphere for the (a) $Pd_{25}Ni_{75}$, (b) $Pd_{50}Ni_{50}$ and (c) $Pd_{75}Ni_{25}$. In red is presented the region with higher electronic density, yellow, medium electronic density, and blue, lower electronic density. (d) Relative increase in particle mean diameter, calculated from the smallest particle enclosing sphere to account for the changes in shape and surface roughness, during H_2 treatment. (e) Relative expansion of the fractal enclosing sphere used to define the outer boundaries of the high density Pd core before and during H_2 treatment in percent. (f) Relative increase in the FWHM value of the curve relative to the electronic density distribution inside the nanoparticles.

In order to validate the conclusions obtained from AP-GIXS analysis, STEM-EELS measurements were performed. Figure 6 shows a typical STEM-HAADF image of the as-prepared $Pd_{25}Ni_{75}$ nanoparticles with around ~ 20 nm diameter and its Pd and Ni compositional maps (see Figure S20 for a typical EELS spectrum). The Ni composition maps (Figure 6(b)) clearly show pockets of Ni-deficient regions in the nanoparticles. These deficient regions are also observed in the O composition map obtained by integrating the O K edge due to the atomic density difference of PdO and NiO (shown in Figure S21). The Pd compositional map (Figure 6(c)) shows the presence of Pd-rich clusters of around 3 to 10 nm size located in the Ni deficient regions. A composite map formed by overlaying the Ni (green) and Pd (magenta) compositional maps is shown in Figure 6(d). It is evident that

multiple pockets of Pd-rich clusters are embedded in the NiO matrix of a single nanoparticle, as validated with several other nanoparticles (Figure S22).

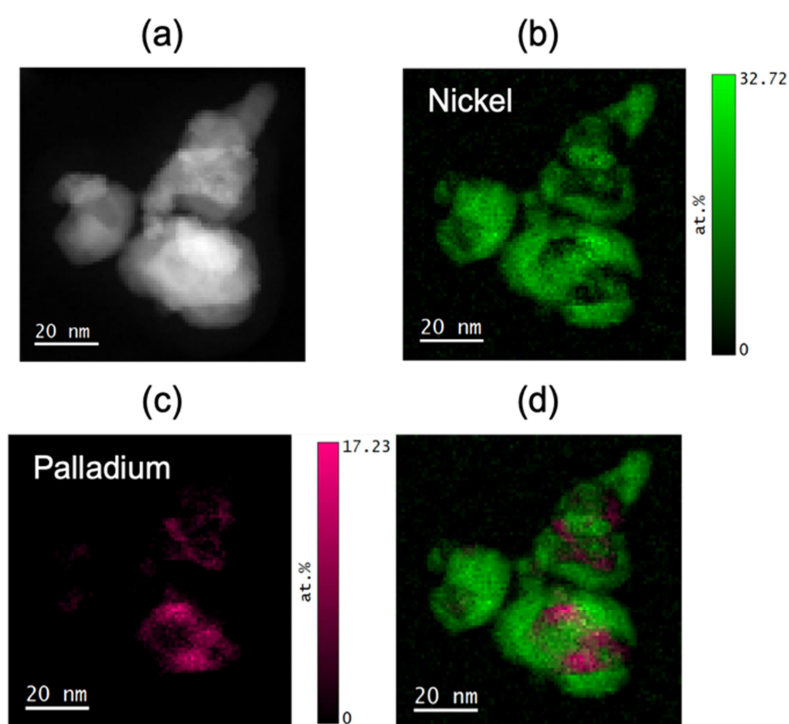


Figure 6: (a) STEM-HAADF image of a typical as prepared $Pd_{23}Ni_{75}$ nanoparticle from which (b) Ni compositional map was obtained by integration of L edge and (c) Pd compositional map was obtained by integration of the M edge. (d) A composite map overlapping the Ni (green) and Pd (magenta) maps. The color bars in these images show the atomic percentage which is calculated based on all the available elements in the spectral window from 230 eV to 1419.3 eV, which includes both C K-edge (~ 284 eV) and O K-edge (~ 532 eV).

All the as-prepared Pd_xNi_{100-x} nanoparticles exhibit an internal structure with a Pd-rich core and Ni-rich shell, as indicated by the compositional difference between bulk-sensitive EDS and surface-sensitive XPS analysis. This phase separation was confirmed by AP-GIXS (Figure 4(d)) and EELS measurements (Figure 6). In addition, it was observed that the as-prepared samples present mainly NiO and PdO compounds. Upon annealing under UHV or exposure to H_2 at RT, Pd in these nanoparticles undergoes reduction from PdO to Pd(0). On the other hand, from the AP-XPS and *in-situ* EXAFS measurements (Figure 2 and 3) it is evident that Ni remains as NiO.

The hydrogen atoms get exclusively adsorbed on the Pd atoms. This is evident from an increase in Pd-Pd distance observed in *in-situ* EXAFS (Figure 2(c)) and an increase in the

FWHM of the Pd(0) peak at Pd 3d AP-XPS measurement under H₂ atmosphere. These increases are proportional to the Pd content in the bimetallic nanoparticles. This is indicative of higher hydrogen adsorption with the increase in Pd content in the nanoparticles. The only exception to this trend is the Pd₂₅Ni₇₅ sample, showing an increase in the Pd-Pd distance and the FWHM of the relative peak of Pd(0) similar to the Pd₇₅Ni₂₅ sample. This might be related to a higher propensity for phase separation of the Pd as observed by AP-GIXS measurements. As a consequence, both the Pd-Pd distance measurements (Figure 2(c)) and relative FWHM increase of the Pd(0) peak at Pd 3d spectra (Figure 3(c)) show a relative minimum at the Pd₅₀Ni₅₀ composition.

In the samples with higher Pd content, the Pd is more dispersed inside the nanoparticles, as observed in the AP-GIXS measurements (Figure S16). This might be either due to the lack of NiO in the nanoparticles to form a proper core-shell structure or to the formation of a solid solution. Theoretical ternary Ni-Pd-O convex hull drawn using the Materials Project (Figure S21) does show Pd₅₀Ni₅₀ (~ 43 meV) close to the stable convex hull.^{31,32} Previous work has shown that such structures might get stabilized at higher temperatures.^{33,34} This stabilization is due to entropic effects which depend critically on how the target alloy composition of interest responds to the temperature effects in contrast to all relevant competing phases.^{35,36} However, to the best of our knowledge, experimental Ni-Pd-O phase diagrams have not been reported till date.

The effect of the phase separation can be visualized by the reconstructed electronic density obtained from the AP-GIXS measurements (Figure 5 (a) and Figure S16). If the Pd₅₀Ni₅₀ composition is stabilized and forms a solid solution, the Pd₇₅Ni₂₅ composition would phase separate into pure Pd rich and Pd₅₀Ni₅₀ regions, thereby explaining the presence of very high Pd-rich regions. However, for both Ni₅₀Pd₅₀ and Pd₂₅Ni₇₅ samples, no Pd rich regions are observed. This is most likely because these compositions are either stable (the case of Pd₅₀Ni₅₀) or the phase separate in the stable Pd₅₀Ni₅₀ and Ni-rich compositions (the case for Pd₂₅Ni₇₅).

From the AP-GIXS measurements, it is evident that during the hydrogen adsorption process, considerable rearrangement of Pd atoms is observed. In general, upon H₂ adsorption, the increase in particle size is in proportion to the Pd content of the nanoparticle. However, the relative Pd pocket expansion and relative distribution compared to the annealed nanoparticles decreases with the increase in the Pd content under the H₂ atmosphere. This is most likely

due to the lack of a well-delineated Pd core in high Pd-containing samples. However, in all cases the hydrogen adsorption leads to a rearrangement of Pd, forming Pd-rich pockets.

Previously, evidence of the atomic rearrangement during hydrogen adsorption process was also observed in a Pd-rich core and Pt-rich shell nanoparticles. Tayal *et al.*³⁷ concluded that the adsorption of hydrogen in this sample transformed the core-shell structure into a mixed Pd-Pt alloy. This process increased the Pd-Pt interfacial area, where the hydrogen was adsorbed, then increasing the hydrogen adsorption capacity of this sample. Similarly, in this work the sample with the smallest amount of Pd presents many small Pd pockets that are very well delimited and segregated from the NiO phase. This process increases the interfacial area between the Pd and NiO phases where the hydrogen can be stored.^{7,37,38}

In fact, a deeper look at the Ni K edge XANES spectra (Figure S22) shows changes in the edge position. In all samples, the introduction of H₂ induces a shift to smaller binding energies, as observed elsewhere.³⁷ It indicates that NiO is not just a bystander during the hydrogen adsorption process, but the hydrogen is adsorbed at the interface between the NiO shell and Pd pockets. It compensates for the small amount of Pd in these nanoparticles, leading to strong changes in the parameters related to hydrogen adsorption from AP-XPS measurements. On the other hand, in Pd-rich nanoparticles, aside from starting to form Pd pockets, this structure is not clearly defined, presenting a diffused transition between Pd pockets and NiO shell. These results indicate that the hydrogen storage process occurs efficiently in these Pd pockets, where a plum pudding-like system is formed. It also reveals the underlying mechanisms, which can be used to reduce the use of noble metals while retaining the H₂ storage capacity in bimetallic nanoparticles.

3. Conclusions

In this work, Pd_xNi_{100-x} nanoparticles were characterized during the hydrogen adsorption process. The use of complementary *in-situ* techniques yielded a more complete picture of the changes affecting the internal structure of nanoparticles. The bimetallic nanoparticles present a Pd-rich core and a Ni-rich shell. It was demonstrated that the H₂ adsorption occurs primarily through interaction with Pd, although slight changes are observed for NiO lattice during the process. However, NiO plays an important role as a separation medium for the

creation of internal Pd pockets. During the hydrogen adsorption, these pockets become further fragmented, creating a larger amount of smaller hydrogen adsorption-active clusters. Even though the overall particle size could decrease during H₂ exposure, these adsorption centers fragment into smaller centers, thus increasing the surface area of Pd available to store hydrogen. These morphological changes observed are invisible through the characterization with conventional techniques but, at the same time, are fundamental for the deep elucidation of the atomic events occurring during the hydrogen storage process. Deeper understanding of the hydrogen adsorption process in these nanoparticles presents a prospective way of making the hydrogen storage tunable, less costly (by using bimetallic systems), and more reliable (by controlling the morphology transformations). Based on our findings, the design of future bimetallic nanoparticles for hydrogen storage could involve an effective medium able to promote the formation of hydrogen adsorption active pockets.

4. Methods

Synthesis

Pd_xNi_{100-x} nanoparticles were synthesized with different compositions, namely Pd₉₀Ni₁₀, Pd₇₅Ni₂₅, Pd₅₀Ni₅₀, and Pd₂₅Ni₇₅. The total mass of nickel chloride hexahydrate plus palladium acetate was kept constant at 92.9 mg in all cases, and its individual values were chosen to achieve the desired Pd/Ni atomic ratios. Initially, nickel chloride hexahydrate (NiCl₂ • 6H₂O) and glucose (0.039g) were totally dissolved in MilliQ® water (7.2 mL), while palladium acetate (Pd(OCOCH₃)₂) was dissolved in monoolein (1-Oleoyl-rac-glycerol technical, ~ 40% purity) (20 g). This mixture was added to an ultrasonic bath for 5 minutes while it was constantly stirred with a spatula. The aqueous solution was added to the mixture containing monoolein and mixed for 1 minute using a spatula. This mixture rested for 10 minutes. After this, it was added to a water bath at 80 °C for 1 hour and mixed with a spatula every 5 minutes. After the bath, the mixture rested for 2 h, and then they were calcined under air at 500 °C for 4 hours, forming a fine dark powder containing the nanostructures.

Transmission Electrons Microscopy (TEM)

TEM measurements were performed at CM-UFGM using a Tecnai G2 Spirit Biotwin microscope operated at 120 kV. For the measurements, the samples' powder was dispersed in

MilliQ® water and left in the ultrasound bath for 15-20 min. Then, three drops of this solution were added to a carbon-coated Cu grid. The size distribution histograms of the Pd_xNi_{100-x} nanoparticles were obtained using ImageJ (Version 6.0) software. The diameter of each nanoparticle was calculated from the total area of its projection in the TEM screen, considering spherical nanoparticles.

Electron Energy Loss Spectroscopy (EELS)

The EELS measurements were performed using the TEAM 1 microscope (double aberration corrected Thermo Fisher Scientific Titan 80-300) at the National Center for Electron Microscopy (NCEM). The EELS dataset was collected at 300 kV using a Gatan Continuum spectrometer, a convergence angle of approximately 30 mrad, and a collection angle of 110 mrad. The width of the zero-loss peak was measured to be 1.2 eV, and a 0.35 eV/channel dispersion was used to collect the spectra. The composition map was obtained by integrating the Ni L edge (L₂ ~ 872 eV and L₃ ~ 855 eV), Pd M edge (M₄ ~ 340 eV and M₅ ~ 335 eV) and O K edge at 532 eV.

X-ray Diffraction (XRD)

The XRD measurements were performed in a Rigaku Ultima IV diffractometer at CNANO-UFRGS using Cu K α (1.5406 Å) radiation and working at 40 kV and 17 mA. Pd_xNi_{100-x} samples were fixed in a glass blade for the XRD measurements. The data were collected for a 2 θ range between 20° and 100°, using a scanning step of 0.05°. Pattern indexing was performed using reference standards obtained from the ICSD database.³⁹ The Rietveld refinement was performed on FullProof⁴⁰ software (version July-2017). The Instrumental Resolution Function (IRF) was obtained from a SiO₂ standard. Rietveld refinements were carried out using the pseudo-Voigt profile function of Thompson, Cox, and Hastings⁴¹ and a linear background. During the refinement, the Debye-Waller overall factor and the atom occupancy were fixed to the crystallographic information file (cif) value obtained from the literature.

X-ray Absorption Spectroscopy (XAS)

The XAS measurements were performed at NOTOS beamline from ALBA Synchrotron Light Source in transmission mode at the Pd K edge (24350 eV) and Ni K edge (8333 eV). For the measurements, the nanoparticles powder was supported over activated carbon

(Activated Charcoal Norit®) with 7 wt% using an ultrasound bath for 20 min. For the Pd K edge and Ni K edge measurements, 13 mm pellets were produced with 75 mg of Pd_xNi_{100-x}/C and 25 mg of BN. For the measurements, the samples were initially exposed to 30 ml/min N₂ and heated to 150 °C where they remained for 15 min. Then, the nanoparticles were cooled down to room temperature (RT) under 30 mL/min He. At RT, the samples were exposed to 30 mL/min of 4% H₂ + 96% He and remained in this condition until its complete stabilization, i.e., until no more changes in the X-Ray Absorption Near Edge Structure (XANES) spectra were observed. The XAS measurements were performed during the full treatment employed. The XANES and EXAFS measurements for Ni K edge were performed integrating 0.24 s/point and with a 0.93 eV and 1 eV energy step, respectively, while for the Pd K edge the integration time was 0.2 s/point and the energy step used was 0.5 eV and 1 eV, respectively. The Extended X-Ray Absorption Fine Structure (EXAFS) spectra were analyzed in accordance with the standard procedure of data reduction⁴² using IFEFFIT.⁴³ The EXAFS signal $\chi(k)$ was extracted, and then Fourier transformed using a k^2 -weighted $\chi(k)$ and a Kaiser-Bessel window with a k -range of 10.0 Å⁻¹ for both edges. The phase shift and amplitudes were obtained with the FEFF6 code by using a fcc metallic Pd, tetragonal PdO, fcc metallic Ni and a fcc NiO cluster with 6 Å radius each. For the fit of the EXAFS oscillations, the amplitude reduction factor (S_0^2) was fixed at 0.85, as obtained from the fit of both Pd(0) and Ni(0) standards. The R-factor obtained from the analysis was always lower than 0.01, which demonstrates the excellent agreement between the proposed model and the experimental result.

Ambient Pressure X-ray Photoelectron Spectroscopy (AP-XPS) and Ambient Pressure Grazing Incidence X-ray Scattering (AP-GIXS)

AP-XPS and AP-GIXS measurements were performed at APPEXS endstation at 11.0.2 beamline of ALS Synchrotron.⁴⁴ For the measurements, the nanoparticles powder was dispersed in ethanol and added to an ultrasonic bath for 10 min. After that, a silicon wafer was covered 3 times with the solution containing the nanoparticles, thus forming a thin layer. After that, the samples were inserted into an ambient pressure reaction chamber, where they were heated to 250 °C under vacuum to clean the sample's surface and to reduce from PdO to Pd(0). Then, the samples were cooled to room temperature, and once at this temperature, they were exposed to 100 mTorr H₂. AP-GIXS measurements were performed for the samples as prepared, after annealing, and during hydrogen exposure. AP-XPS measurements were

performed before and after every AP-GIXS measurement. For the AP-XPS measurements, a SPECS PHOIBOS 150 NAP analyzer was used, with a photon beam energy of 1000 eV and 695 eV. Energy regions collected were survey, Pd 3d, Ni 3p, Pd 4p, Si 2p, C1s, and O1s. A step of 1 eV and 0.1 eV, dwell time of 0.2 s, and pass energy of 10 eV were used for the survey and high-resolution spectra, respectively.

KOLXPD software (v. 1.8.0) was used for the XPS analysis. For the fitting of the high-resolution spectra, a Shirley-type background was used. The fitting procedure, shown in Figure S15, was performed by fixing the distance between Pd(0) and PdO and Pd(0) satellite at 1.3 eV⁴⁵ and 6.7 eV,⁴⁶ respectively. An asymmetric Doniach Sunjic peak was used for the fit of the Pd(0) component, and Voigt peaks were used for all the other chemical components. The Gaussian width of the peaks was fixed at the same value for all the peaks. The Lorentzian width was fixed for the same component in all the measured conditions, except for the Pd(0), where asymmetry was fixed.

For the AP-GIXS measurements, a beam energy of 1240 eV, corresponding to a wavelength of 1 nm was used. The total collection solid angle was +/-12° in-plane and 24° out of plane, which translates to $q_{\text{max}} \sim 0.9 \text{ nm}^{-1}$ and 1.8 nm^{-1} , respectively. Andor iKon-L CCD mounted on the biaxial quasi-spherical manipulator was used to collect scattered photons. To minimize the influence of the silica substrate GIXS analysis was performed on a horizontal line-cut extracted directly above the Yoneda-line at a scattering vector (q) of 0.2 nm^{-1} .²⁵ The PDDF was obtained from the inverse fourier transform of the horizontal line-cut utilizing the BioXTAS RAW software package (see Note S2 for details on GIXS line cuts and analysis).⁴⁷⁻⁴⁹ The electron density reconstruction was performed utilizing the BIOXTAS RAW and the integrated DENS package (details on the reconstruction are found in Note S2).²⁸

AP-XPS was also performed at APXPS endstation at 9.3.2 beamline of ALS Synchrotron. The nanoparticles were prepared in the same way presented for the measurements at 11.0.2. The nanoparticles were inserted into an ambient pressure chamber and heated to 700 °C under vacuum. Pd 3d and Ni 3p energy regions were measured during the heating process. After that, the nanoparticles were cooled down to room temperature where they were exposed to 1×10^{-7} mTorr, 1×10^{-5} mTorr, 1×10^{-3} mTorr, 1×10^{-1} mTorr and 5×10^{-1} mTorr of H₂. At each pressure, energy regions collected were survey, Pd 3d, Ni 3p, Pd 4p, Si 2p, C1s, and O1s. All the measurements were performed using a 695 eV photon beam energy, a pass energy of 20 eV, dwell time of 100 ms and step size of 0.1 eV and 0.5 were used for the high-resolution

and survey spectra.

Scanning Electrons Microscopy (SEM) and Energy Dispersive Spectroscopy (EDS)

SEM images and EDS spectra were obtained at Molecular Foundry-LBL using a Zeiss Gemini Ultra-55 microscope operated with 5 kV. The samples were measured before and after the AP-XPS and AP-GIXS measurements. The SEM images were obtained by detecting secondary electrons.

Atomic Force Microscopy (AFM)

AFM measurements were conducted at the Imaging Facility of the Molecular Foundry-LBL using a Asylum Jupyter AFM, and a PEAKFORCE-HIRS-F-A tip from BrukerNano. The AFM was operated in tapping mode, with a drive amplitude of 100 mV and a setpoint of 60 mV. Scan speed was set to 0.75 lines per second and the resolution to 256 x 256 lines x rows.

Supporting Information

Supporting Information is available from the Wiley Online Library or from the author.

Acknowledgements

This research used APPEXS endstation at beamlines 9.3.2 and 11.0.2.1 of the Advanced Light Source, which is a DOE Office of Science User Facility under contract no. DE-AC02-05CH11231. The authors thank ALBA Synchrotron staff for the measurements performed at NOTOS (BL-16) beamline (proposal 2021095397). The authors also thank CNANO-UFRGS and CM-UFMG staff for their assistance. This study was funded by FAPERGS (19/2551-0001752-9 and 19/2551-0000703-5), CNPq (310142/2021-0) and CAPES (Finance Code 001). L. P. M. and F. B. thank the CNPq for the research grant. L.P.M. thanks CAPES for the research grant. C.E. thanks the MICINN-FEDER funding through the PID2021-124572OB-C33 grant. Work at the Molecular Foundry was supported by the Office of Science, Office of Basic Energy Sciences, of the U.S. Department of Energy under Contract No. DE-AC02-05CH11231.

Conflict of Interest Statement

The authors declare no conflict of interest.

References

1. Karpa, W. & Grginović, A. (not so) stranded: The case of coal in Poland. *Energies* **14**, 8476 (2021).
2. Mazloomi, K. & Gomes, C. Hydrogen as an energy carrier: Prospects and challenges. *Renew. Sustain. Energy Rev.* **16**, 3024–3033 (2012).
3. *DOE Technical Targets for Onboard Hydrogen Storage for Light-Duty Vehicles.* (2017).
4. Usman, M. R. Hydrogen storage methods: Review and current status. *Renew. Sustain. Energy Rev.* **167**, 112743 (2022).
5. Jena, P. Materials for hydrogen storage: Past, present, and future. *J. Phys. Chem. Lett.* **2**, 206–211 (2011).
6. Konda, S. K. & Chen, A. Palladium based nanomaterials for enhanced hydrogen spillover and storage. *Mater. Today (Kidlington)* **19**, 100–108 (2016).
7. Chen, B. W. J. & Mavrikakis, M. Effects of composition and morphology on the hydrogen storage properties of transition metal hydrides: Insights from PtPd nanoclusters. *Nano Energy* **63**, 103858 (2019).
8. Thill, A. S. *et al.* A new non-complex synthesis of NiO nanofoams for hydrogen storage applications. *Mater. Adv.* **4**, 476–480 (2023).
9. Ren, J., Liao, S. & Liu, J. Hydrogen storage of multiwalled carbon nanotubes coated with Pd-Ni nanoparticles under moderate conditions. *Chin. Sci. Bull.* **51**, 2959–2963 (2006).
10. Sano, N., Taniguchi, K. & Tamon, H. Hydrogen storage in porous single-walled carbon nanohorns dispersed with Pd-Ni alloy nanoparticles. *J. Phys. Chem. C Nanomater. Interfaces* **118**, 3402–3408 (2014).

11. Campesi, R. *et al.* In situ synthesis and hydrogen storage properties of PdNi alloy nanoparticles in an ordered mesoporous carbon template. *Microporous Mesoporous Mater.* **117**, 511–514 (2009).
12. Militello, M. C. & Simko, S. J. Palladium oxide (PdO) by XPS. *Surf. Sci. Spectra* **3**, 395–401 (1994).
13. Chen, L. F. *et al.* Hydrogen spillover and structural defects in a PdO/zirconia nanophase synthesized through a surfactant-templated route. *J. Alloys Compd.* **417**, 220–223 (2006).
14. Figueiredo, W. T. *et al.* New insights on the electronic factor of the SMSI effect in Pd/TiO₂ nanoparticles. *Appl. Surf. Sci.* **574**, 151647 (2022).
15. Matte, L. P. *et al.* Influence of the CeO₂ support on the reduction properties of Cu/CeO₂ and Ni/CeO₂ nanoparticles. *J. Phys. Chem. C Nanomater. Interfaces* **119**, 26459–26470 (2015).
16. Mavrikakis, M., Hammer, B. & Nørskov, J. K. Effect of strain on the reactivity of metal surfaces. *Phys. Rev. Lett.* **81**, 2819–2822 (1998).
17. Tew, M. W., Miller, J. T. & van Bokhoven, J. A. Particle size effect of hydride formation and surface hydrogen adsorption of nanosized palladium catalysts: L₃ edge vs K edge X-ray absorption spectroscopy. *J. Phys. Chem. C Nanomater. Interfaces* **113**, 15140–15147 (2009).
18. Oumellal, Y., Provost, K., Ghimbeu, C. M., de Yuso, A. M. & Zlotea, C. Composition and size dependence of hydrogen interaction with carbon supported bulk-immiscible Pd-Rh nanoalloys. *Nanotechnology* **27**, 465401 (2016).
19. Bird, R. J. & Swift, P. Energy calibration in electron spectroscopy and the re-determination of some reference electron binding energies. *J. Electron Spectros. Relat. Phenomena* **21**, 227–240 (1980).
20. Mejías, J. A. *et al.* Interpretation of the binding energy and auger parameter shifts found by XPS for TiO₂ supported on different surfaces. *J. Phys. Chem.* **100**, 16255–16262 (1996).
21. Mansour, A. N. Characterization of NiO by XPS. *Surf. Sci. Spectra* **3**, 231–238 (1994).

22. Bennett, P. A. & Fuggle, J. C. Electronic structure and surface kinetics of palladium hydride studied with x-ray photoelectron spectroscopy and electron-energy-loss spectroscopy. *Phys. Rev. B Condens. Matter* **26**, 6030–6039 (1982).
23. Yeh, J. J. & Lindau, I. Atomic subshell photoionization cross sections and asymmetry parameters: $1 \leq Z \leq 103$. *At. Data Nucl. Data Tables* **32**, 1–155 (1985).
24. Ruban, A. V., Skriver, H. L. & Nørskov, J. K. Surface segregation energies in transition-metal alloys. *Phys. Rev. B Condens. Matter* **59**, 15990–16000 (1999).
25. Schwartzkopf, M. *et al.* From atoms to layers: in situ gold cluster growth kinetics during sputter deposition. *Nanoscale* **5**, 5053 (2013).
26. Guinier, G. *Small-Angle Scattering of X-Rays*. (John Wiley & Sons, New York, 1955).
27. Schnablegger, H. & Singh, Y. *The SAXS Guide*. (Anton Paar GmbH, Graz, 2023).
28. Grant, T. D. Ab initio electron density determination directly from solution scattering data. *Nat. Methods* **15**, 191–193 (2018).
29. Liao, H., Fisher, A. & Xu, Z. J. Surface segregation in bimetallic nanoparticles: A critical issue in electrocatalyst engineering. *Small* **11**, 3221–3246 (2015).
30. Anitas, E. M. Small-angle scattering from fractals: Differentiating between various types of structures. *Symmetry (Basel)* **12**, 65 (2020).
31. Jain, A. *et al.* Commentary: The Materials Project: A materials genome approach to accelerating materials innovation. *APL Mater.* **1**, (2013).
32. Ong, S. P., Wang, L., Kang, B. & Ceder, G. Li–Fe–P–O₂ phase diagram from first principles calculations. *Chem. Mater.* **20**, 1798–1807 (2008).
33. Aykol, M., Dwaraknath, S. S., Sun, W. & Persson, K. A. Thermodynamic limit for synthesis of metastable inorganic materials. *Sci. Adv.* **4**, (2018).
34. Bartel, C. J. *et al.* Physical descriptor for the Gibbs energy of inorganic crystalline solids and temperature-dependent materials chemistry. *Nat. Commun.* **9**, 4168 (2018).

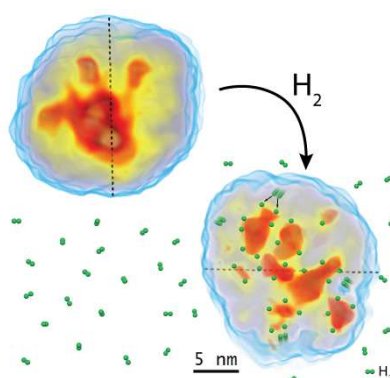
35. van de Walle, A. & Ceder, G. The effect of lattice vibrations on substitutional alloy thermodynamics. *Rev. Mod. Phys.* **74**, 11–45 (2002).
36. Kapoor, V., Singh, B., Sai Gautam, G., Cheetham, A. K. & Canepa, P. Rational design of mixed polyanion electrodes $\text{Na}_x\text{V}_2\text{P}_{3-i}(\text{Si/S})_i\text{O}_{12}$ for sodium batteries. *Chem. Mater.* **34**, 3373–3382 (2022).
37. Tayal, A. *et al.* Mechanism of hydrogen storage and structural transformation in bimetallic pd–pt nanoparticles. *ACS Appl. Mater. Interfaces* **13**, 23502–23512 (2021).
38. Yamauchi, M., Kobayashi, H. & Kitagawa, H. Hydrogen storage mediated by Pd and Pt nanoparticles. *Chemphyschem* **10**, 2566–2576 (2009).
39. Bergerhoff, G. & Berndt, M. Inorganic structural chemistry with crystallographic databases. *Acta Crystallogr. A* **52**, C314–C314 (1996).
40. Rodríguez-Carvajal, J. Recent advances in magnetic structure determination by neutron powder diffraction. *Physica B Condens. Matter* **192**, 55–69 (1993).
41. Thompson, P., Cox, D. E. & Hastings, J. B. Rietveld refinement of Debye–Scherrer synchrotron X-ray data from Al_2O_3 . *J. Appl. Crystallogr.* **20**, 79–83 (1987).
42. Koningsberger, D. *et al.* Fundamental Principles and Data Analysis. 143–155 (2000).
43. Ravel, B. & Newville, M. *ATHENA, ARTEMIS, HEPHAESTUS*: data analysis for X-ray absorption spectroscopy using *IFEFFIT*. *J. Synchrotron Radiat.* **12**, 537–541 (2005).
44. Kersell, H. *et al.* Simultaneous ambient pressure x-ray photoelectron spectroscopy and grazing incidence x-ray scattering in gas environments. *Rev. Sci. Instrum.* **92**, (2021).
45. Pillo, T., Zimmermann, R., Steiner, P. & Hüfner, S. The electronic structure of PdO found by photoemission (UPS and XPS) and inverse photoemission (BIS). *J. Phys. Condens. Matter* **9**, 3987–3999 (1997).
46. Militello, M. C. & Simko, S. J. Elemental palladium by XPS. *Surf. Sci. Spectra* **3**, 387–394 (1994).
47. Putnam, C. D., Hammel, M., Hura, G. L. & Tainer, J. A. X-ray solution scattering (SAXS) combined with crystallography and computation: defining accurate

macromolecular structures, conformations and assemblies in solution. *Q. Rev. Biophys.* **40**, 191–285 (2007).

48. Jacques, D. A. & Trehwella, J. Small-angle scattering for structural biology—Expanding the frontier while avoiding the pitfalls. *Protein Sci.* **19**, 642–657 (2010).

49. Feigin, L. *Structure Analysis by Small-Angle X-Ray and Neutron Scattering*. (1987).

Table of Contents



The complex atomic mechanism of hydrogen storage in bimetallic nanoparticles is elucidated through meticulous experiments. Bimetallic Ni-Pd nanoparticles present a Pd-rich core and NiO-rich shell structure. This structure suffers a transformative process under H₂ atmosphere with the creation of Pd pockets that enhance the hydrogen uptake capacity. It opens new possibilities for the design of advanced materials for hydrogen storage.

Supporting Information

Direct observation of phase change accommodating hydrogen uptake in bimetallic nanoparticles

Lívia P. Matte,¹ Maximilian Jaugstetter,² Tara P. Mishra,³ Carlos Escudero,⁴ Giuseppina Conti,^{5,6} Slavomir Nemsak,^{5,6} Fabiano Bernardi^{1,*}*

¹ *Programa de Pós-Graduação em Física, Instituto de Física, Universidade Federal do Rio Grande do Sul (UFRGS), Porto Alegre, RS, 91501-970, Brazil*

² *Chemical Sciences Division, Lawrence Berkeley National Laboratory, Berkeley, CA, 94720, USA*

³ *Materials Science Division, Lawrence Berkeley National Laboratory, Berkeley, CA, 94720, USA*

⁴ *ALBA Synchrotron Light Source, Cerdanyola del Vallès, Barcelona, 08290, Spain*

⁵ *Advanced Light Source, Lawrence Berkeley National Laboratory, Berkeley, CA, 94720, USA*

⁶ *Department of Physics and Astronomy, University of California, Davis, CA, 95616, USA*

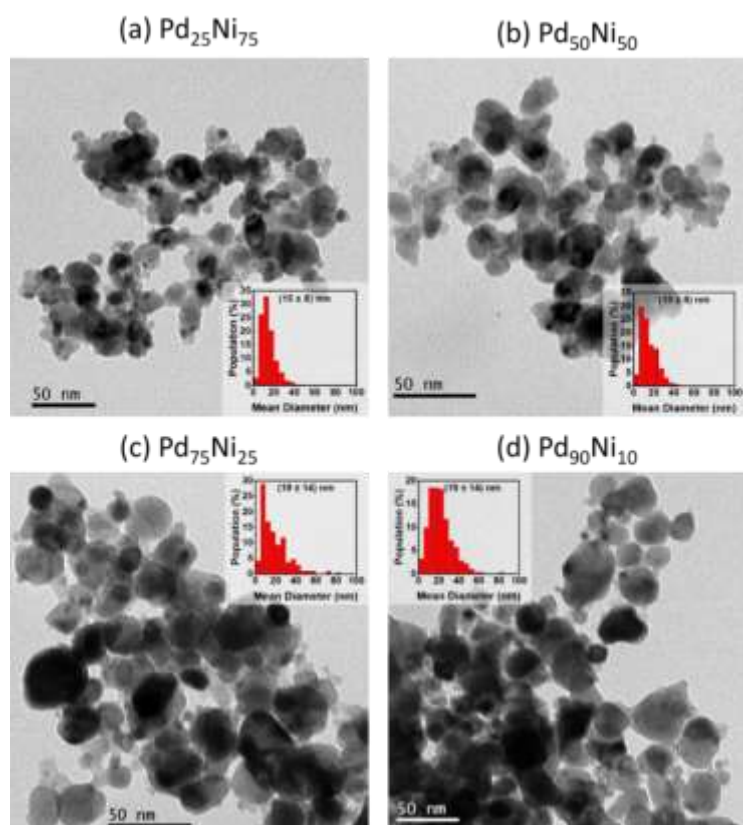


Figure S1: Typical TEM images of the (a) $\text{Pd}_{25}\text{Ni}_{75}$, (b) $\text{Pd}_{50}\text{Ni}_{50}$, (c) $\text{Pd}_{75}\text{Ni}_{25}$, and (d) $\text{Pd}_{90}\text{Ni}_{10}$ nanoparticles. The inset shows the histogram of size distribution.

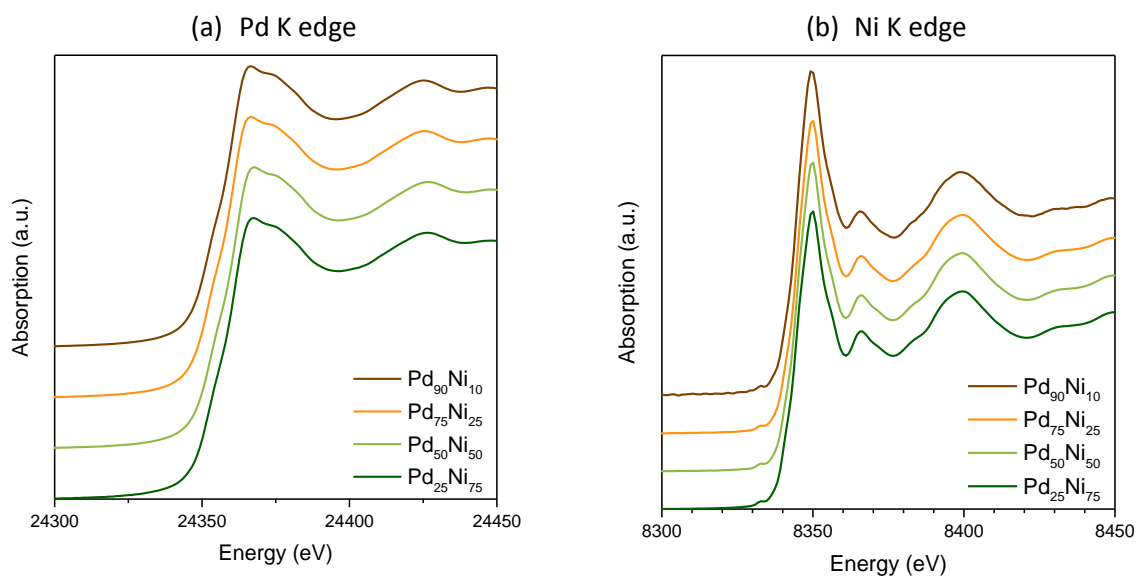


Figure S2: XANES measurements of the as-prepared samples at the (a) Pd K edge and (b) Ni K edge.

Table S1: Comparison between the nanoparticles mean diameter obtained from the TEM images and the crystallite size obtained from the XRD diffractograms.

	XRD (crystallite size)			TEM (mean diameter)
	NiO	PdO	Pd	
Pd ₂₅ Ni ₇₅	18 nm	19 nm		(15 ± 8) nm
Pd ₅₀ Ni ₅₀	8 nm	13 nm		(15 ± 8) nm
Pd ₇₅ Ni ₂₅	20 nm	26 nm	29 nm	(19 ± 14) nm
Pd ₉₀ Ni ₁₀		23 nm	33 nm	(19 ± 14) nm

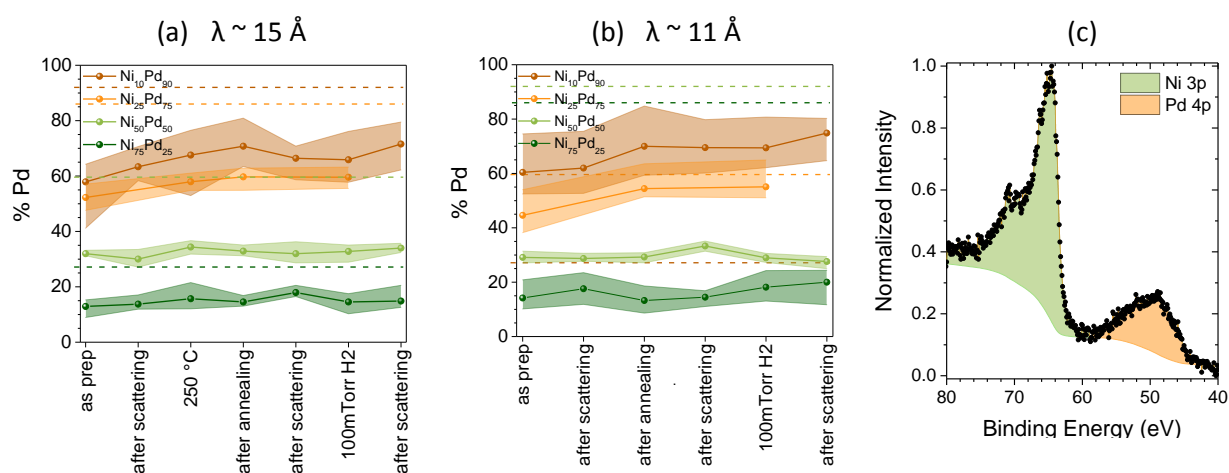


Figure S3: Pd percentage in the surface of the nanoparticles considering two different depths probed with (a) $\lambda \sim 15 \text{ \AA}$ ($h\nu = 1000 \text{ eV}$) and (b) $\lambda \sim 11 \text{ \AA}$ ($h\nu = 695 \text{ eV}$) obtained from the shaded area presented in (c), where the orange and green areas represent the Pd 4p and Ni 3p energy regions, respectively. The main lines in figures (a) and (b) represent the mean value obtained after 5 analysis process, while the shaded areas include all the values obtained. The brown line represents the value obtained for the Pd₉₀Ni₁₀, orange represents the Pd₇₅Ni₂₅, light green represents the Pd₅₀Ni₅₀, and dark green represents the Pd₂₅Ni₇₅ nanoparticles. The dashed lines represent the value obtained by EDS.

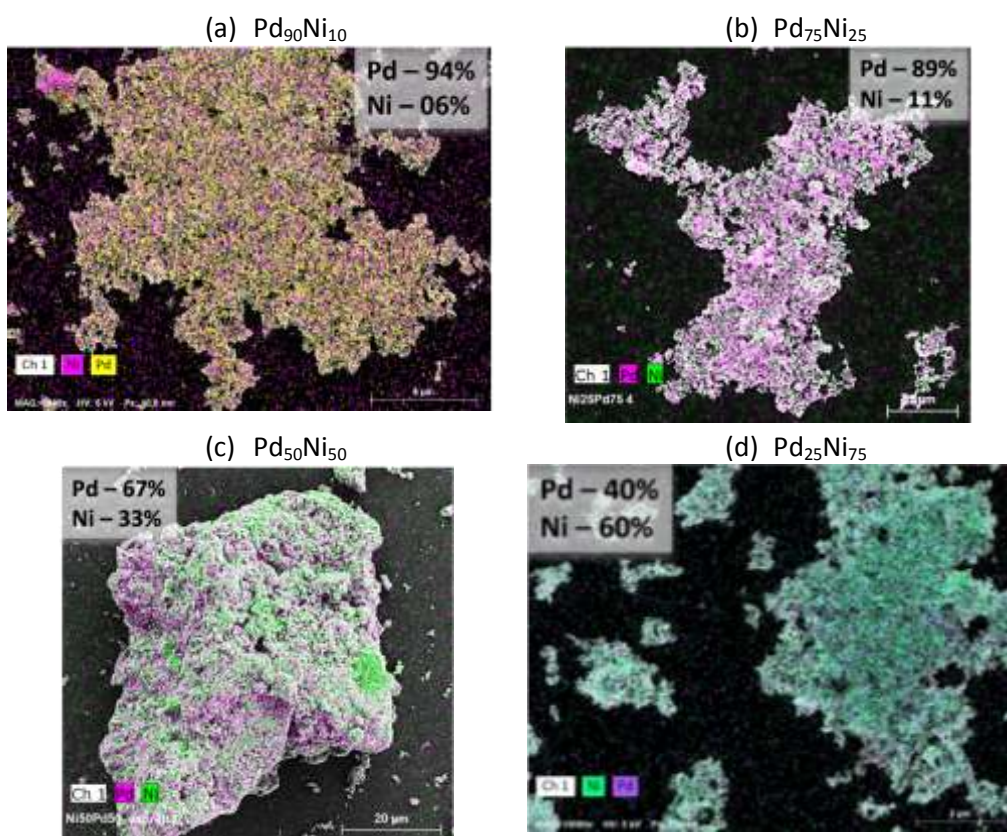


Figure S4: EDS maps of the different Ni_xPd_{100-x} bimetallic nanoparticles studied. The Pd and Ni fraction for each sample is shown in the inset.

Figure S5 shows the time evolution of the XANES spectra measured at room temperature while the samples were exposed to 30 mL/min 4% H₂ + 96% He. Initially, all the samples present one intense peak after the absorption edge, which is characteristic of PdO XANES spectrum. During the exposure to H₂ atmosphere, most of the samples evolve and their XANES spectra present a change from one to two peaks near the absorption edge. These two peaks are characteristic of a Pd(0) XANES spectrum, then indicating the samples' reduction. However, this evolution is not observed for the sample with the highest amount of Ni (Pd₂₅Ni₇₅), which still exhibits only one peak after the absorption edge, indicating a high amount of PdO in this sample. In addition, the samples present different reduction times depending on the Pd fraction in the nanoparticles (the higher the Pd content the fastest the reduction).

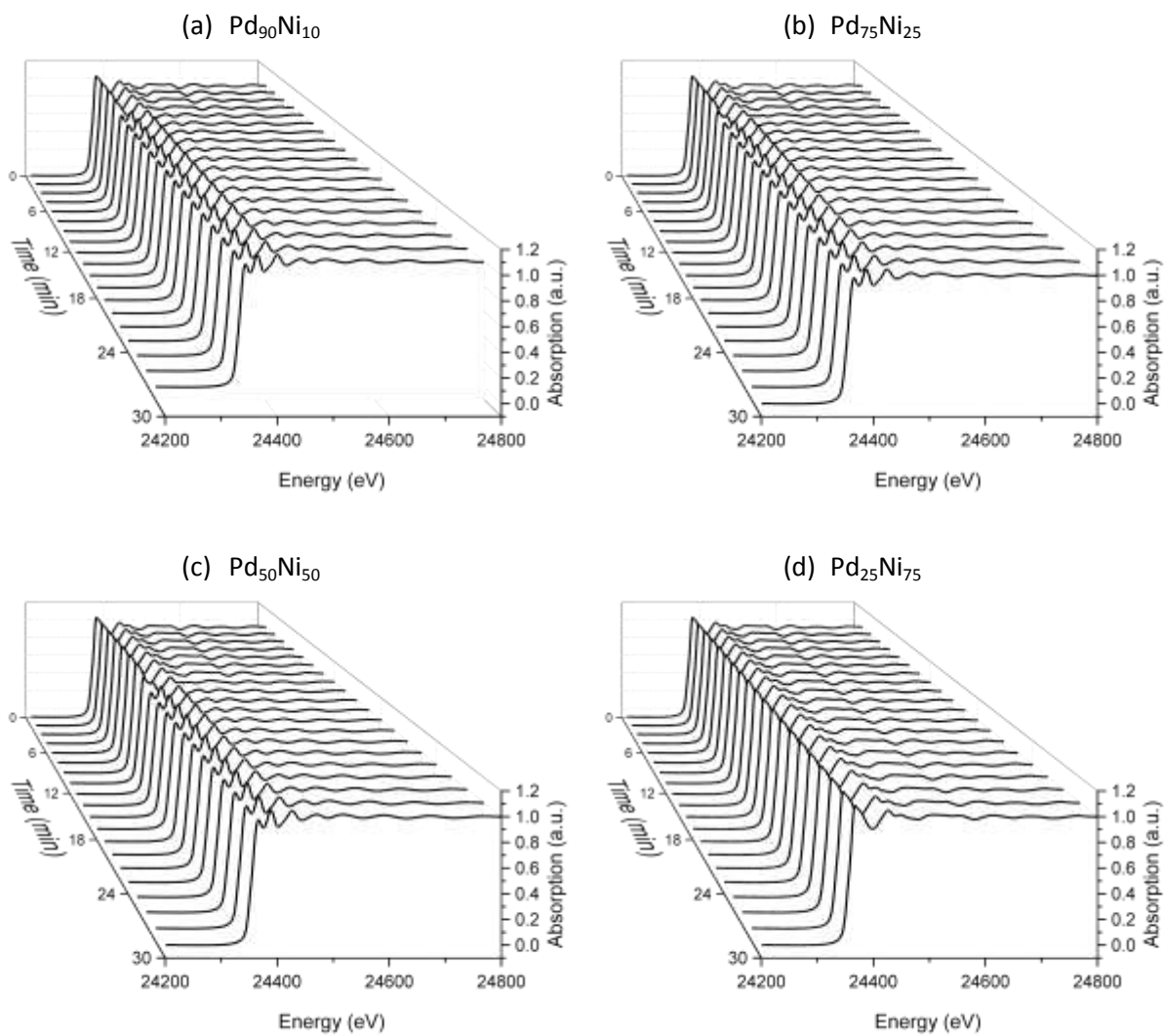
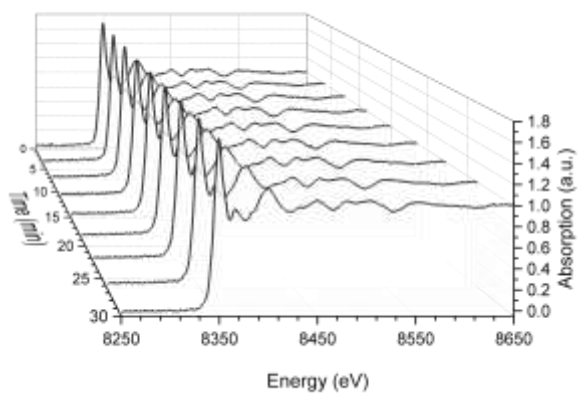
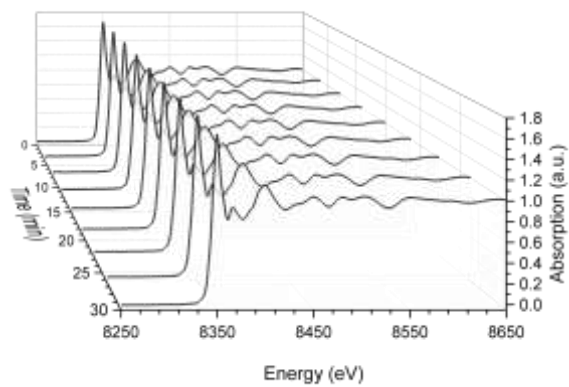


Figure S5: Time-resolved XANES spectra at Pd K edge during exposure to 30 mL/min 4% H₂ + 96% He at RT under atmospheric pressure.

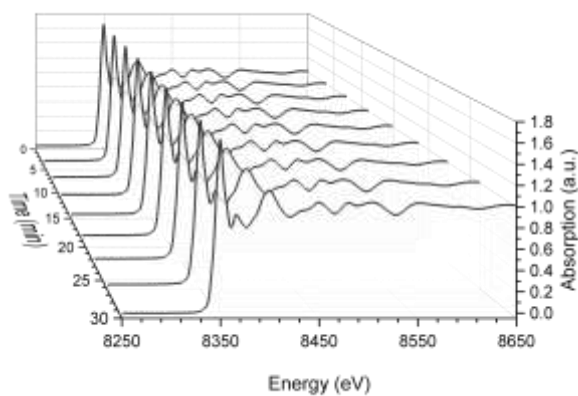
(a) Pd₉₀Ni₁₀



(b) Pd₇₅Ni₂₅



(c) Pd₅₀Ni₅₀



(d) Pd₂₅Ni₇₅

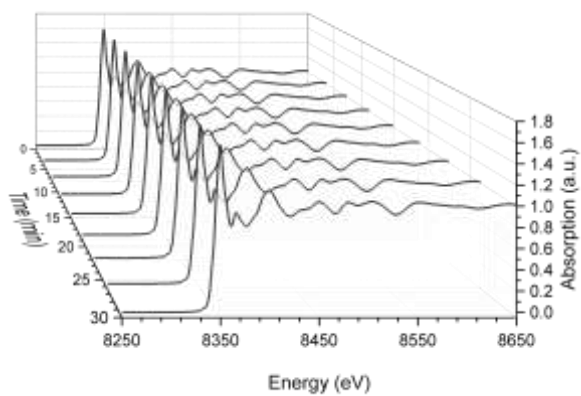


Figure S6: Time-resolved XANES spectra at Ni K edge during exposure to 30 mL/min 4% H₂ + 96% He at RT under atmospheric pressure.

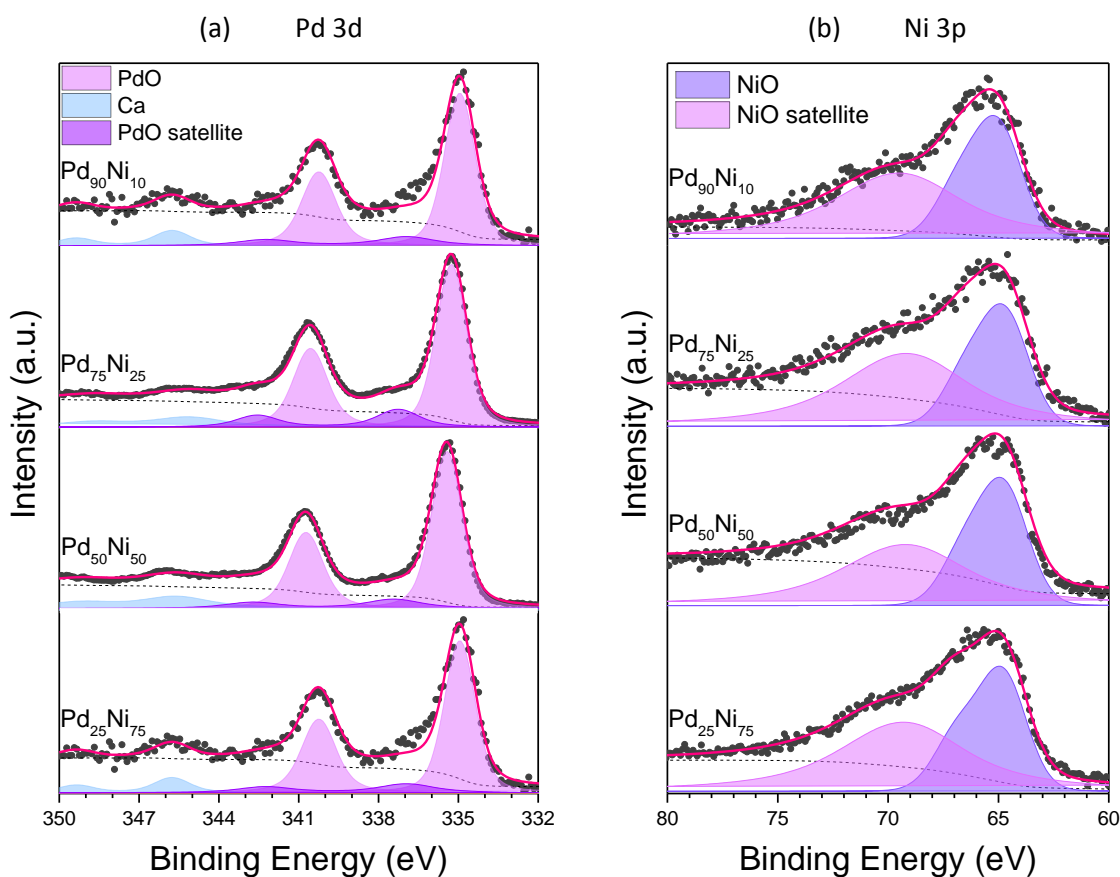


Figure S7: XPS measurements of the as-prepared nanoparticles in the (a) Pd 3d and (b) Ni 3p region. The black dots represent the data measured, the pink line represents the fit performed and the shaded area the component as shown inset in the figure.

Figure S8 presents the XPS spectra of the Pd 3d region as a function of temperature. For the measurements, the samples were heated to 700 °C under vacuum. All the as-prepared sample, present only one Pd component related to PdO, showing that their surface is fully oxidized, as expected. During the heating treatment, it is observed the reduction of the PdO to Pd(0). For the Pd₉₀Ni₁₀ sample, this reduction starts before 300 °C, where two components are observed in the Pd 3d spectra. However, the full reduction of the Pd atoms does not occur before reaching 600 °C. On the other hand, for the Pd₂₅Ni₇₅ sample, the Pd atoms on the surface reduce almost completely before reaching 400 °C.

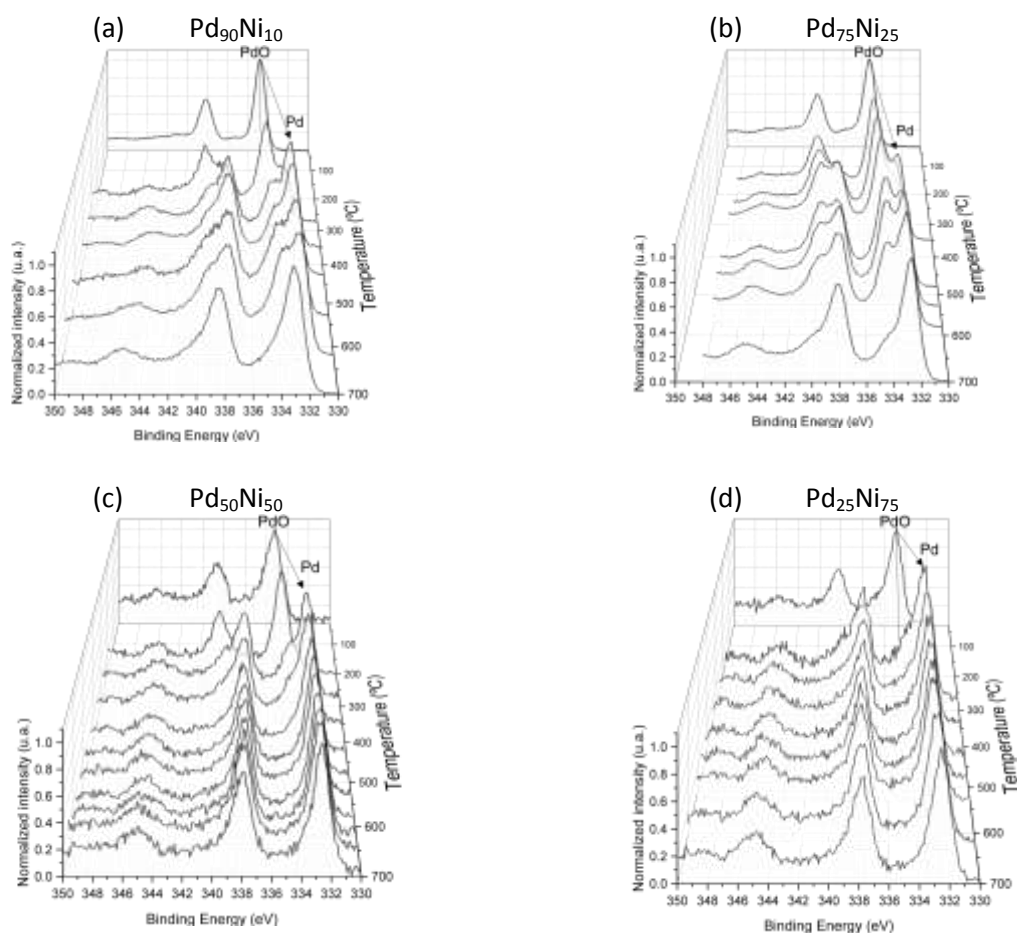


Figure S8: XPS spectra at the Pd 3d energy region as a function of the temperature measured during the heating process under vacuum of the nanoparticles using a beam energy of 695 eV for the (a) $\text{Pd}_{90}\text{Ni}_{10}$, (b) $\text{Pd}_{75}\text{Ni}_{25}$, (c) $\text{Pd}_{50}\text{Ni}_{50}$ and, (d) $\text{Pd}_{25}\text{Ni}_{75}$ samples.

Figure S9 shows the EXAFS oscillations and the corresponding FT measured at Ni K edge for the samples under three conditions: as prepared, at 150 °C under N_2 , and at RT under H_2 (all measurements done at atmospheric pressure). It is observed that all the FT are similar to the NiO standard case, presenting Ni-O and Ni-Ni scattering paths, indicating the Ni atoms are fully oxidized. Besides, no big difference is observed in the FT when the condition is changed, *i.e.*, the as prepared, at 150 °C, and the sample under H_2 present very similar FTs. A similar effect is observed for the as-prepared and at 150 °C sample measured in the Pd K edge (Figure S10). The as-prepared samples present Pd-O and Pd-Pd scattering peaks related to a PdO cluster, indicating the Pd atoms in the samples are fully oxidized. In addition, the position and intensity of the peaks are similar between the samples, *i.e.*, they are independent of the amount of Pd inside the nanoparticles. In the first two steps, the samples present almost

no change. However, when exposed to an H_2 atmosphere, the sample reduces, and the FT becomes similar to the Pd(0) standard.

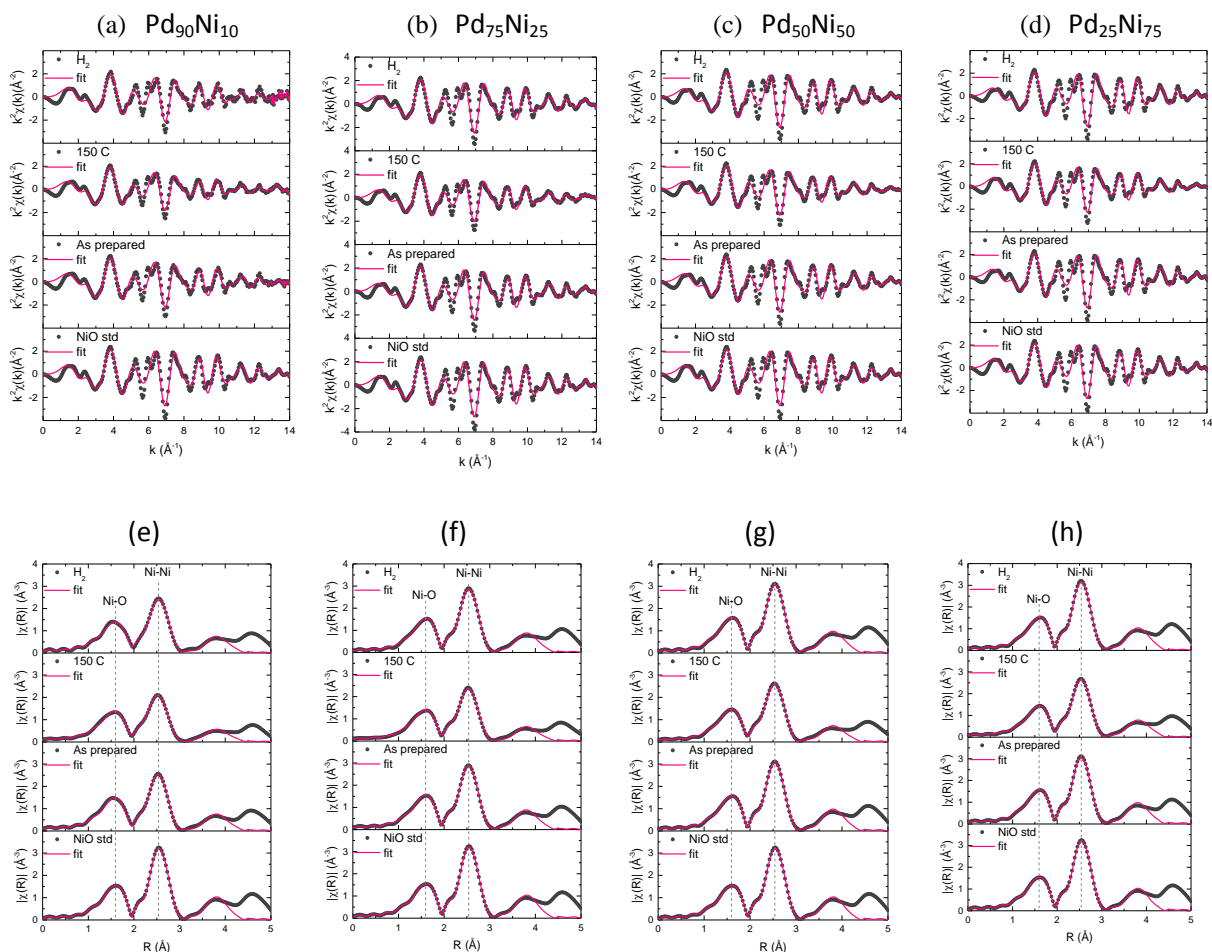


Figure S9: EXAFS oscillations at Ni K edge and the respective FT for the (a) $Pd_{90}Ni_{10}$, (b) $Pd_{75}Ni_{25}$ (c) $Pd_{50}Ni_{50}$ and, (d) $Pd_{25}Ni_{75}$ nanoparticles. The graphics present, from bottom to up: NiO standard, as prepared, at 150 °C under 30 mL/min N_2 , and at RT under 30 mL/min 4% H_2 + 96 % He (all at atmospheric pressure). The dots represent the data measured, while the pink line represents the fit performed.

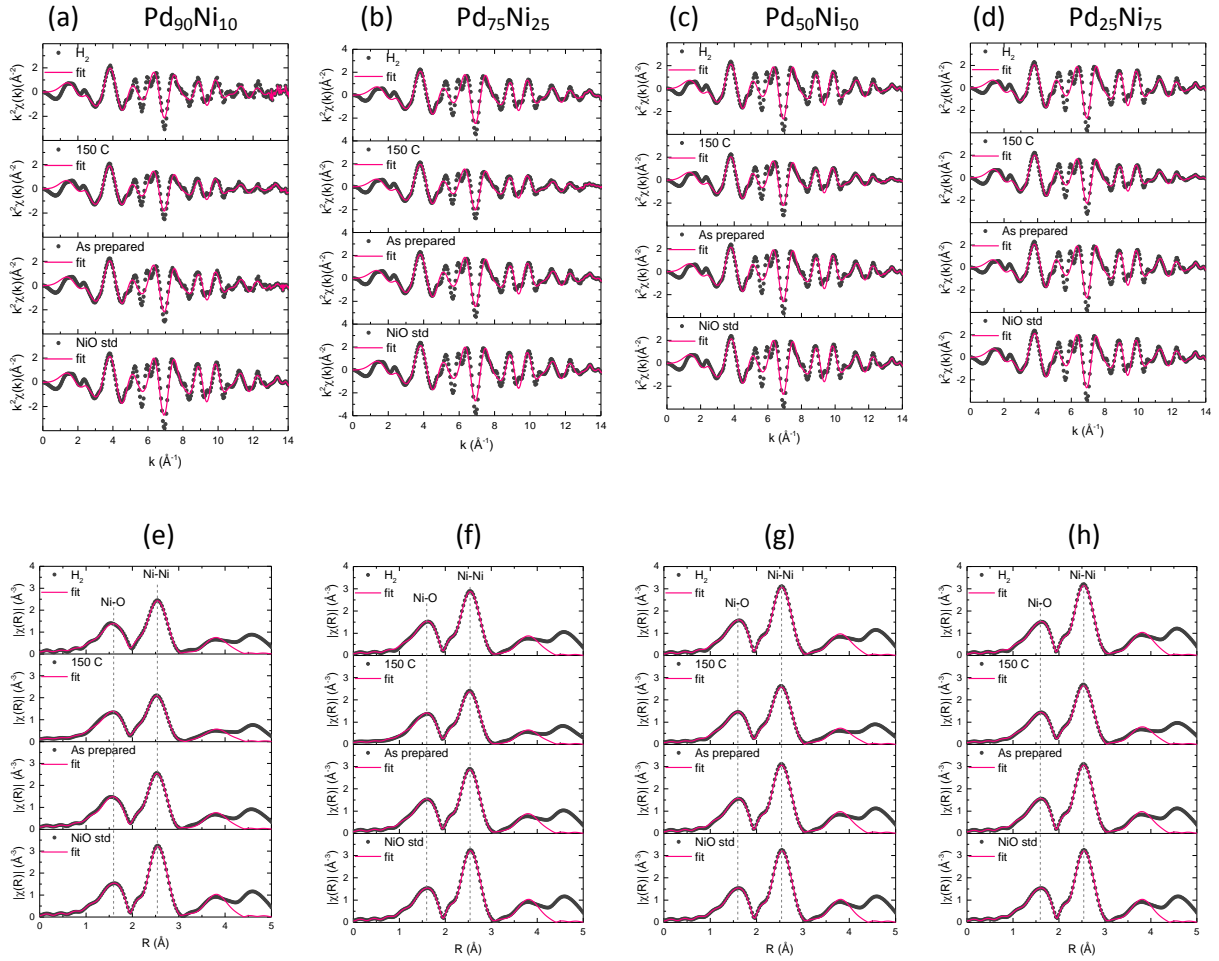


Figure S10: EXAFS oscillations at Pd K edge and the respective FT for the (a) Pd₉₀Ni₁₀, (b) Pd₇₅Ni₂₅ (c) Pd₅₀Ni₅₀ and, (d) Pd₂₅Ni₇₅ nanoparticles. The graphics present, from bottom to up: Pd standard, as prepared, at 150 °C under 30 mL/min N₂, and at RT under 30 mL/min 4% H₂ + 96 % He (all at atmospheric pressure). The dots represent the data measured, while the pink line represents the fit performed.

Table S2: Parameters obtained from the quantitative analysis of the in-situ EXAFS data measured at the Pd K edge for the bimetallic nanoparticles during exposure to H₂ at atmospheric pressure.

Scattering Path		Pd(0) standard	Pd ₉₀ Ni ₁₀	Pd ₇₅ Ni ₂₅	Pd ₅₀ Ni ₅₀	Pd ₂₅ Ni ₇₅
	N	12	11.2 ± 0.2	10.0 ± 0.2	9.4 ± 0.2	8.3 ± 0.2
Pd-Pd	R (Å)	2.772 ± 0.001	2.818 ± 0.002	2.805 ± 0.002	2.776 ± 0.002	2.803 ± 0.001
	σ ² (Å ²)	0.0057 ± 0.0001	0.0083 ± 0.0002	0.0099 ± 0.0002	0.0090 ± 0.0002	0.0087 ± 0.0001

Table S3: Parameters obtained from the quantitative analysis of the in-situ EXAFS data measured at the Ni K edge for the bimetallic nanoparticles during exposure to H₂ at atmospheric pressure.

Scattering Path		NiO standard	Pd ₉₀ Ni ₁₀	Pd ₇₅ Ni ₂₅	Pd ₅₀ Ni ₅₀	Pd ₂₅ Ni ₇₅
Ni-O	N	6	6.000 ± 0.002	5.9 ± 0.2	5.9 ± 0.2	5.6 ± 0.2
	R (Å)	2.075 ± 0.003	2.071 ± 0.004	2.077 ± 0.003	2.077 ± 0.003	2.077 ± 0.003
	σ ² (Å ²)	0.0062 ± 0.0005	0.0081 ± 0.0006	0.0061 ± 0.0005	0.0057 ± 0.0005	0.0055 ± 0.0005
Ni-Ni	N	12	11.5 ± 0.3	12.000 ± 0.3	12.000 ± 0.008	12.000 ± 0.008
	R (Å)	2.962 ± 0.001	2.960 ± 0.002	2.962 ± 0.001	2.960 ± 0.001	2.957 ± 0.001
	σ ² (Å ²)	0.0065 ± 0.0001	0.0086 ± 0.0002	0.0073 ± 0.0002	0.0068 ± 0.0002	0.0066 ± 0.0002

NOTE 1

Figures S11 and S12 present the AP-XPS measurements performed after annealing at 250 °C and during the exposure to 100 mTorr H₂ at RT. In Figure S11 and S12, as well as in Figure 2 of the main text, the spectra were subtracted from a constant value in order to have zero as the lower value in each spectrum. In addition, the maximum value in all spectra was normalized to 1. This procedure was performed aiming to facilitate the visualization of the difference in each pair of spectra related to changes in the sample, thus removing the influence of the H₂ atmosphere in the intensity of the peaks. The difference presented in Figure 11 and 12 (and Figure 2, main text) was obtained by subtracting the spectrum with 100 mTorr H₂ at RT from the annealed one under UHV. In all samples, the annealed spectra presented were measured right before the exposure to H₂. This means that the spectra used were measured after almost 2h of the sample at RT. The exception is the Pd₇₅Ni₂₅ sample, which was measured right when the sample achieved RT.

An observed effect in the Pd 3d energy region are small shifts in the Pd(0) component towards higher binding energies after H₂ exposure (see Figure S11). Interestingly, a shift in the opposite direction is observed when a lower photon energy is used (see Figure S12). The same is not observed in the Ni 3p energy region for the samples with lower Ni content, where no difference is observed between the spectra before and after H₂ exposure. However, for Pd₂₅Ni₇₅ nanoparticles, the Ni 3p region shifts to higher binding energies in the measurements performed with a photon energy of 695 eV (see Figure S12 II-(d)). It is important to note that the absolute binding energy values and shifts for suspended nanoparticles are not always

indicative of a chemical change. The electrostatic alignment between the particle and substrate can result in apparent shifts, as we believe is the case here as well.

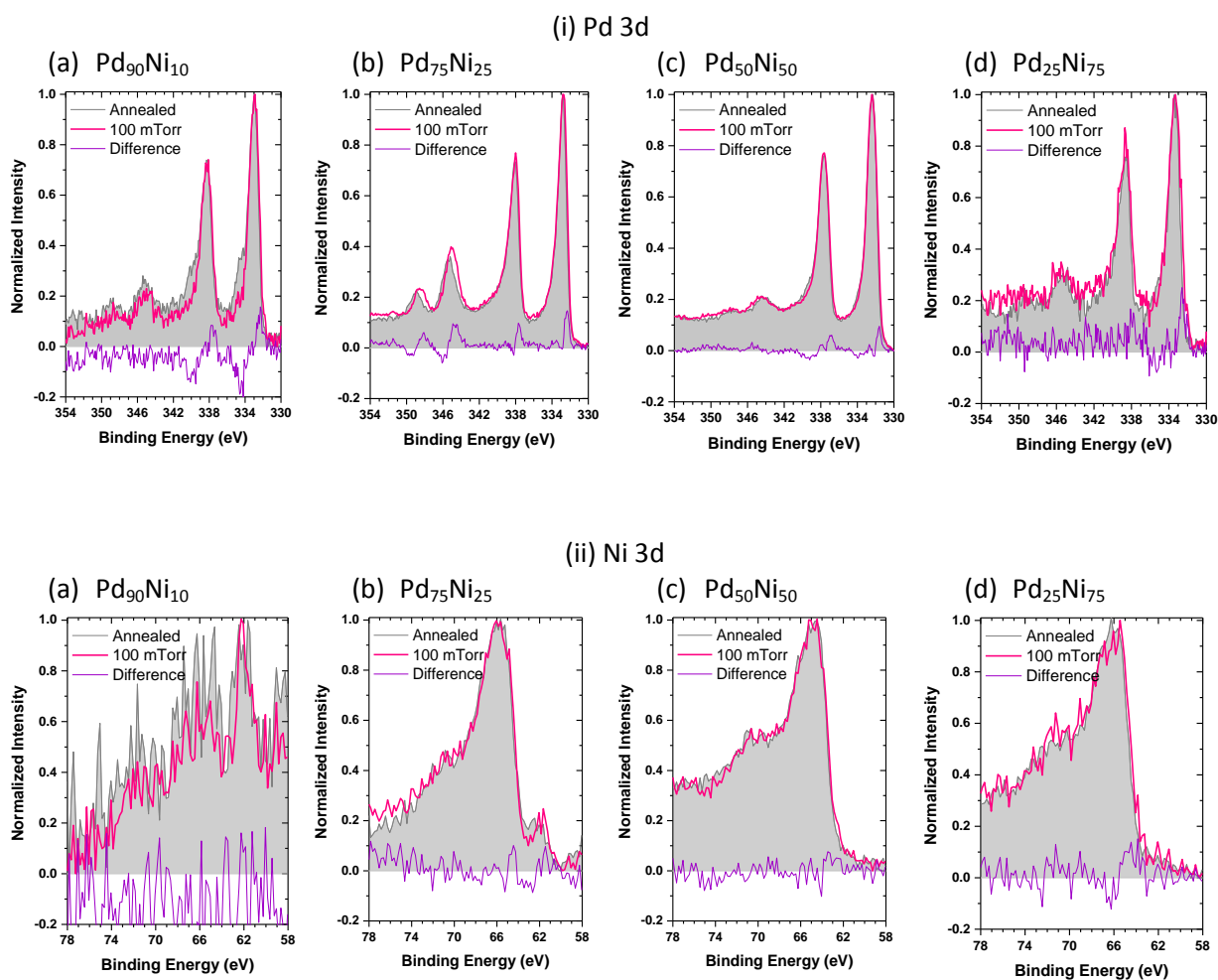


Figure S11: AP-XPS measurements of the (a) $\text{Pd}_{90}\text{Ni}_{10}$, (b) $\text{Pd}_{75}\text{Ni}_{25}$, (c) $\text{Pd}_{50}\text{Ni}_{50}$, and (d) $\text{Pd}_{25}\text{Ni}_{75}$ in the (I) Pd 3d and (II) Ni 3p energy regions using a photon energy of 1000 eV. The solid line represents the spectrum after annealing (gray) and during the exposure to 100 mTorr of H_2 at RT for 2h (pink). The difference between the spectrum during the H_2 exposure process and the spectrum measured after annealing is presented in purple.

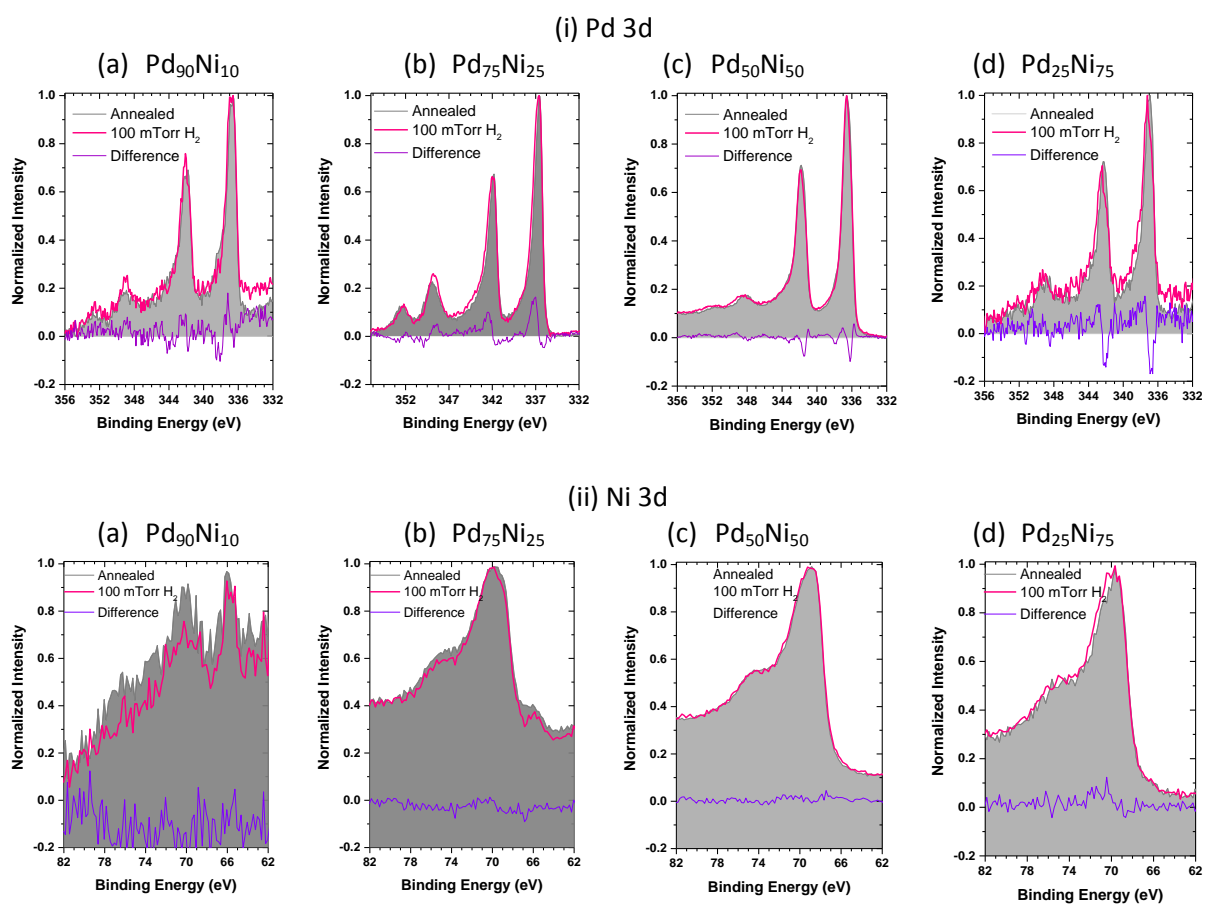


Figure S12: AP-XPS measurements of the (a) $\text{Pd}_{90}\text{Ni}_{10}$, (b) $\text{Pd}_{75}\text{Ni}_{25}$, (c) $\text{Pd}_{50}\text{Ni}_{50}$, and (d) $\text{Pd}_{25}\text{Ni}_{75}$ in the (I) Pd 3d and (II) Ni 3p energy regions using a photon energy of 695 eV. The solid line represents the spectrum after annealing (gray) and during the exposure to 100 mTorr of H_2 at RT for 2h (pink). The difference between the spectrum during the H_2 exposure process and the spectrum measured after annealing is presented in purple.

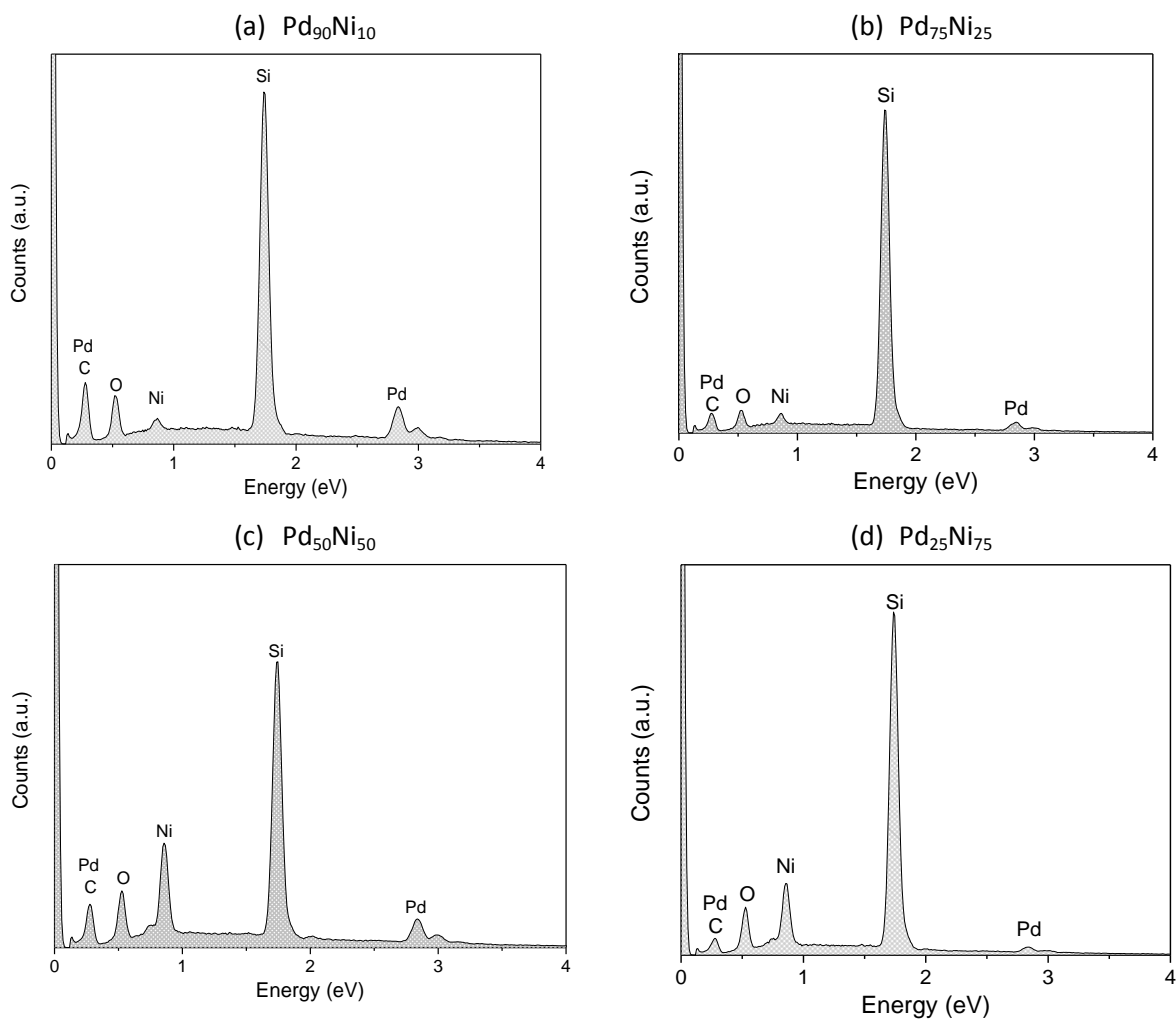


Figure S13: EDS spectra of the as-prepared (a) $\text{Pd}_{90}\text{Ni}_{10}$, (b) $\text{Pd}_{75}\text{Ni}_{25}$, (c) $\text{Pd}_{50}\text{Ni}_{50}$ and (d) $\text{Pd}_{25}\text{Ni}_{75}$. The Si signal comes from the support used for the samples.

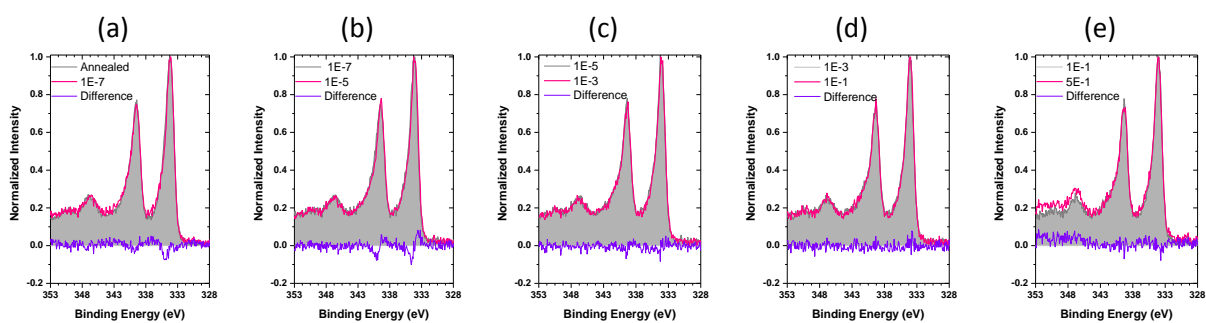


Figure S14: Pd 3d spectra of the $\text{Pd}_{50}\text{Ni}_{50}$ nanoparticles measured by increasing the H_2 pressure to (a) 1×10^{-7} torr H_2 , (b) 1×10^{-5} torr H_2 , (c) 1×10^{-3} torr H_2 , (d) 1×10^{-1} torr H_2 and (e) 5×10^{-1} torr H_2 . The pink line represents the spectra measured with a higher H_2 pressure, the gray shaded area represents the spectra measured with a lower pressure, and the purple line represents the difference between the measurements. These measurements were performed using a photon energy of 695 eV. The spectra were treated in the same way described in Figure 10.

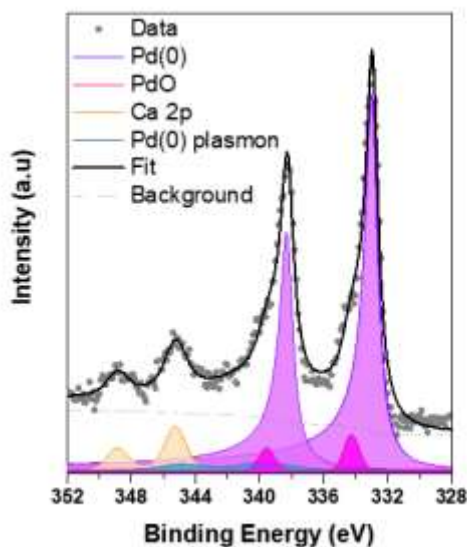


Figure S15: Typical fitting procedure applied to the Pd 3d XPS spectra for Pd₉₀Ni₁₀ after the cleaning process performed under vacuum at 250 °C.

Table S4: FWHM values of the main Pd(0) component obtained from the fitting procedure of the AP-XPS spectra measured after annealing (before H₂ exposure) and during 100 mTorr H₂ exposure for 2 h at RT using a 1000 eV or 695 eV photon energy.

	1000 eV		695 eV	
	Annealed	100 mTorr H ₂	Annealed	100 mTorr H ₂
Pd ₉₀ Ni ₁₀	0.90	1.18	0.81	1.04
Pd ₇₅ Ni ₂₅	0.88	0.98	0.73	0.89
Pd ₅₀ Ni ₅₀	1.05	1.18	0.97	1.06
Pd ₂₅ Ni ₇₅	1.02	1.34	0.90	1.16

NOTE 2:

The AFM images show that the Pd-Ni particles with higher Pd content tend to agglomerate less than respective particles with higher content. The normal distribution gives for Pd₇₅Ni₂₅, mean = 26.7 nm, SD = 10.1 nm, Pd₅₀Ni₅₀, mean = 22.6 nm, SD = 8.5 nm, Pd₂₅Ni₇₅, mean = 26.3 nm, SD = 6.6 nm. These data were used for initial simulations of the particle scattering pattern using BornAgain.¹

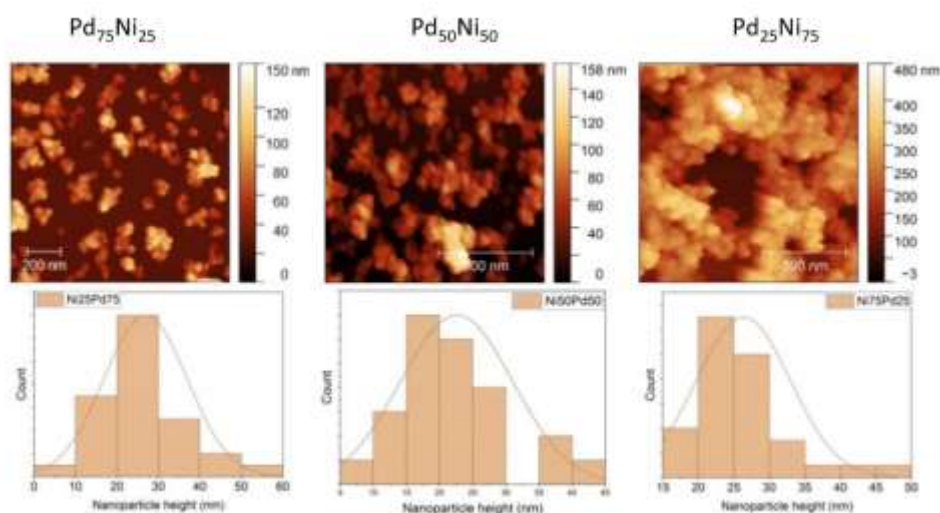


Figure S16: AFM height measurements of the nanoparticle decorated Si wafer used to obtain the GIXS scattering curves. Distribution curves are collected for particle height only and include only particles that are directly adsorbed to the substrate.

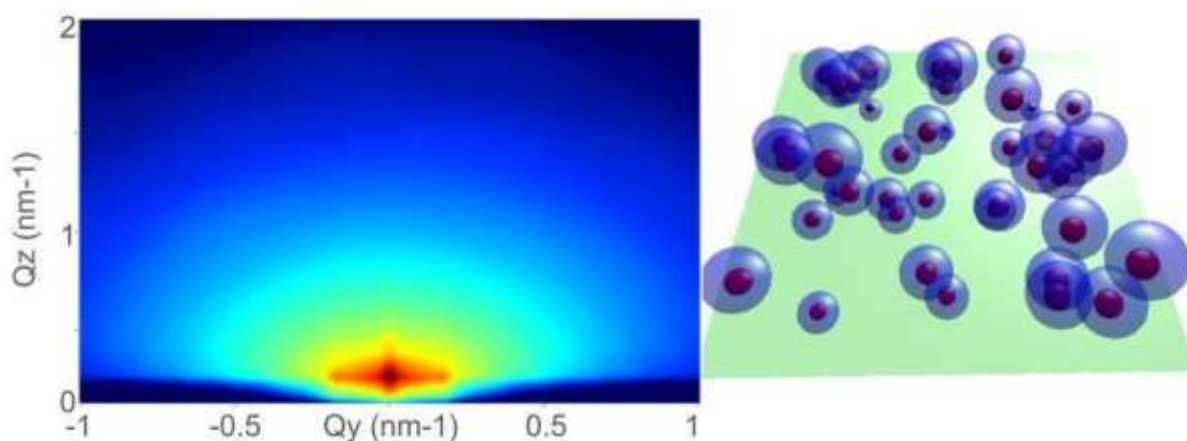


Figure S17: Simulation of scattering spectra using BornAgain. Left simulated scattering pattern. Right used model with the substrate depicted in green the Ni shell depicted in blue and the Pd core depicted in red.

To verify the validity of the obtained scattering patterns we simulated the geometry obtained by AFM utilizing the input model of BornAgain. The particle size was set to 25 nm and the standard deviation to 8.5 nm. Particle and substrate optical parameters were extracted utilizing the Optical properties tool from the Center for X-ray Optics (CXRO: https://henke.lbl.gov/optical_constants/pert_form.html) for Pd, Ni, and Si at the used photon energy of 1240 eV. Core was set to an equivalent radius of 5 nm, which corresponds to the Pd content of the Pd₂₅Ni₇₅ particles. All simulated geometries show the scattering pattern

depicted in Figure S17. As modeling with programs such as BornAgain does not account for inhomogeneities in density within an individual form factor. Pair distance distributions (PDDF) were drawn from the out of plane line scans through the origin, to obtain information on the particle composition and shape.

The 3d electron reconstruction by GIXS may be obtained from the measurement of an object in many different angles, due to the use of many nanoparticles, this is obtained from one typical measurement.² We confirmed using GIXS simulations that the particles are not ordered in a defined pattern, therefore the derived form factor is not influenced by a structure factor. The out of plane cut was used to utilize the random stacking of particles sitting on other particles instead of the substrate to mimic the unoriented particle assemblies typically observed in SAXS. The electron density reconstruction was performed in the Fourier transformed GIXS curve as described in Ref 3. This electron reconstruction is not unique, since it is based on modeling. However, many tests were done with different line cuts and similar results were obtained. In addition, besides the symmetry break of the GIXS measurements, this method initially described to SAXS is still valid.

As the total amount of electrons for each reconstruction is limited to 200 the following statements can be made for this density distributions: The higher the average density per voxel the higher the difference between the electron dense core and the shell of the nanoparticles. The higher the standard deviation the further these regions of higher density are distributed within the particle core. The electron density distributions show that the density difference between core and shell in Pd₇₅Ni₂₅ and Pd₂₅Ni₇₅ is roughly similar but way higher for Pd₅₀Ni₅₀.

Table S5: Bulk electron density values for Pd, PdO, Ni, and NiO.

Bulk material	Electronic density
Pd	3.06 e/Å ³
Ni	2.67 e/Å ³
PdO	2.16 e/Å ³
NiO	1.96 e/Å ³

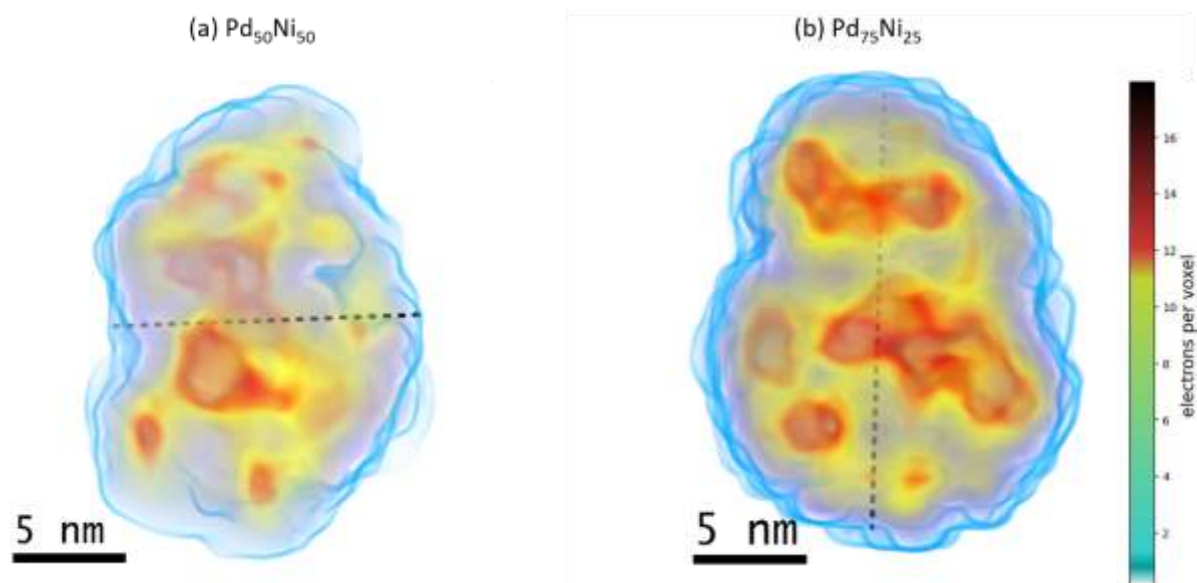


Figure S18: Reconstruction of the electronic density after annealing for the (a) $\text{Pd}_{50}\text{Ni}_{50}$ and (b) $\text{Pd}_{75}\text{Ni}_{25}$. In red is presented the region with higher electronic density, yellow, medium electronic density, and blue, lower electronic density.

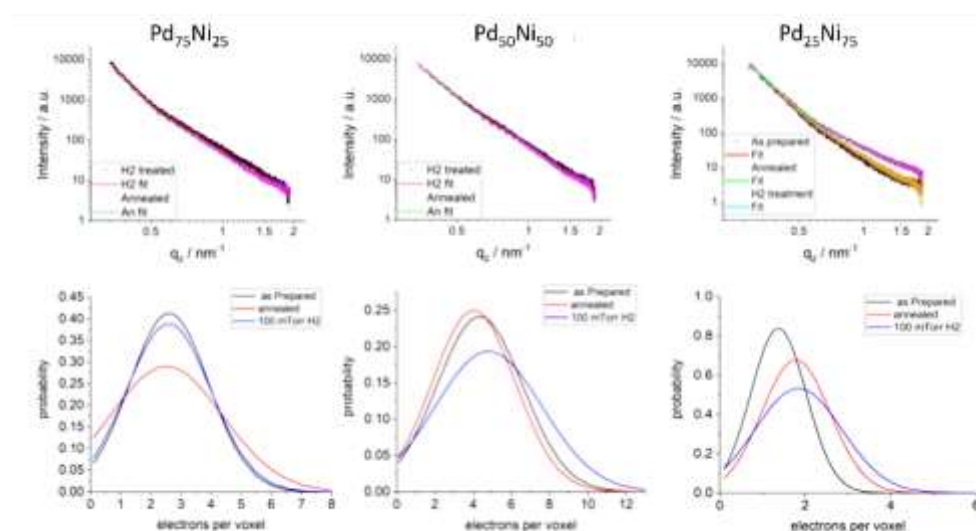


Figure S19: Taken out of plane line cuts for the different Pd-Ni nanoparticles at all three conditions, together with the fits used to obtain the PDDFs for electron density reconstructions (Top). Distribution of electron densities within the reconstructed nanoparticles using the DENS method (bottom) only voxels with electron density higher than 10% of the maximum density are considered.

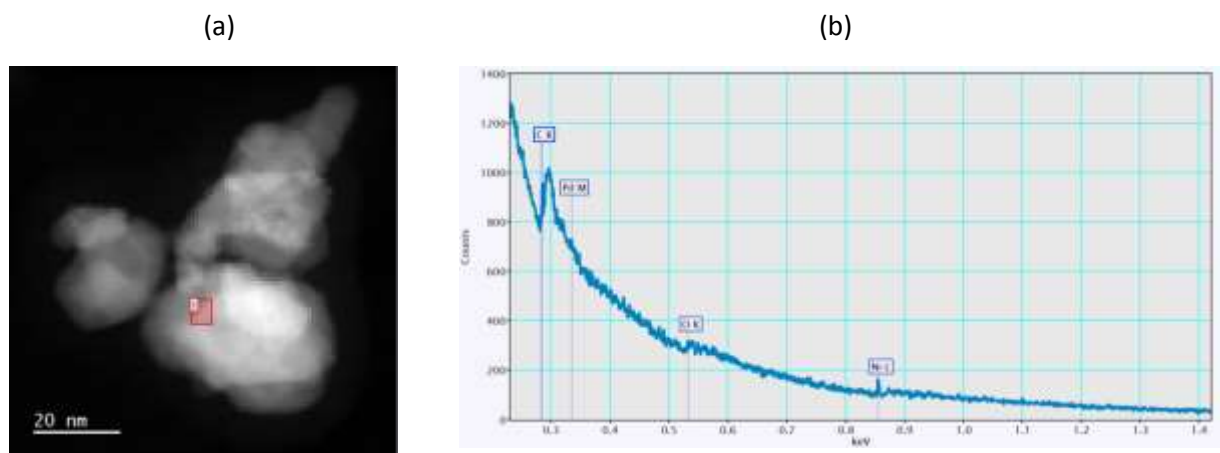


Figure S20: (a) STEM-HAADF image of the $\text{Pd}_{25}\text{Ni}_{75}$ nanoparticles and (b) Typical EELS spectrum from the marked region in (a).

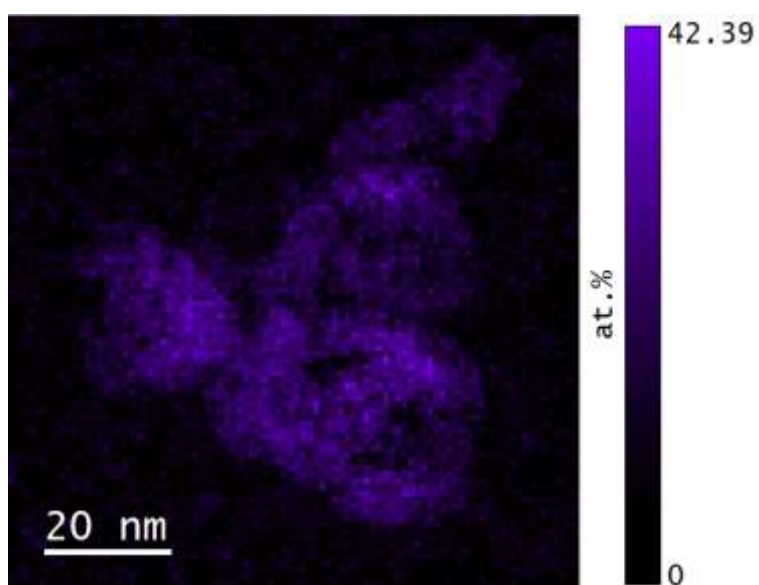


Figure S21: Oxygen compositional map from the EELS spectrum obtained from the particle shown in figure 6 of main text by integrating the Oxygen K edge at 532 eV.

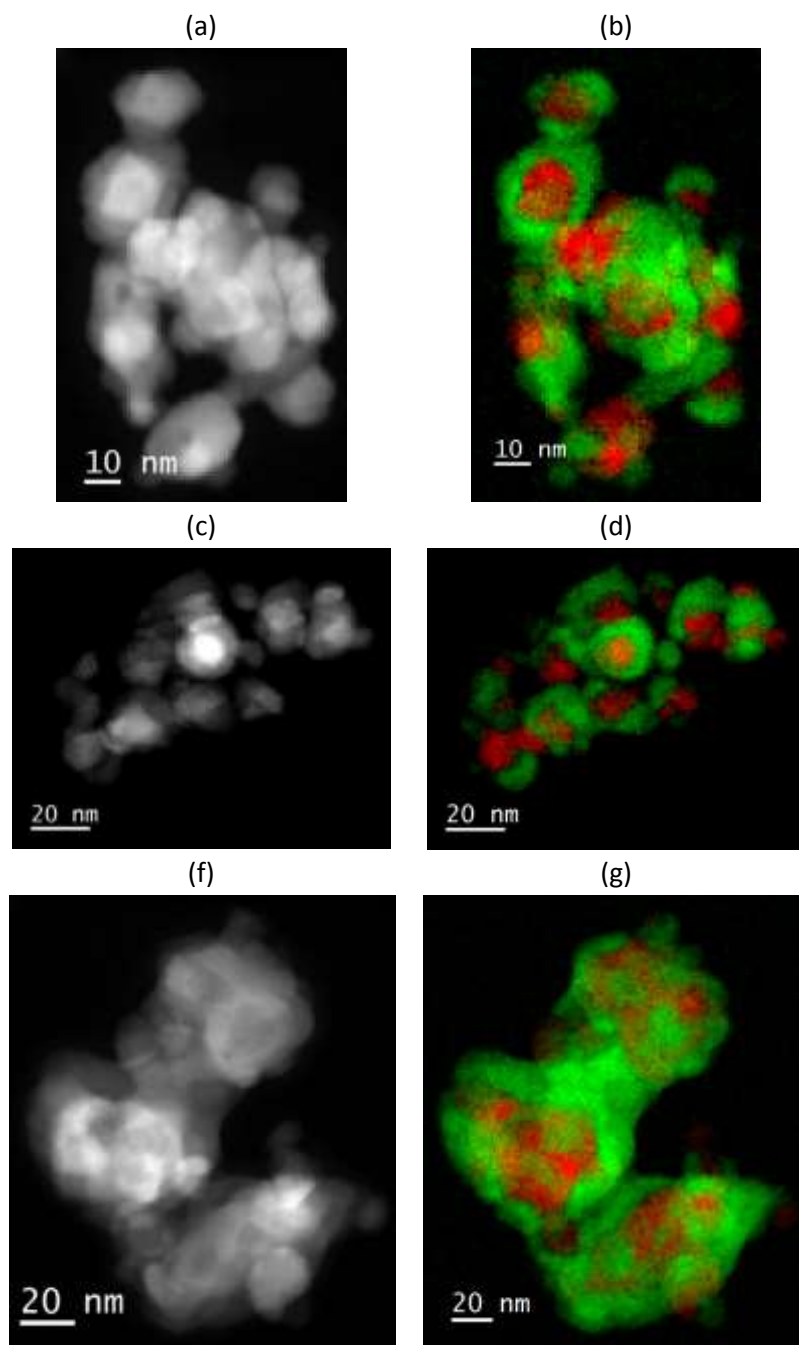


Figure S22: Compositional mapping of as-prepared $\text{Pd}_{25}\text{Ni}_{75}$ nanoparticles obtained using STEM-EELS. On the left is presented the STEM-HAADF image while on the right side a composite map of Ni (green) and Pd (red) obtained from the Ni and Pd composition maps is presented.

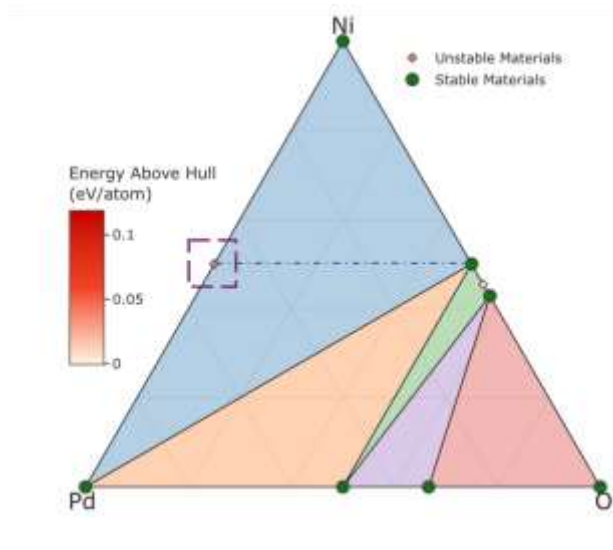


Figure S23: Pd-Ni-O ternary convex hull obtained from the materials project. These convex hulls are calculated using the *r2SCAN* functional. The stable phases are shown as green dots and unstable phases are marked as diamonds. The tie lines connecting the stable phases are marked as black lines. The color of the diamonds indicates the energy above the hull. The phases $\text{Pd}_{50}\text{Ni}_{50}$ are marked in blue dashed box. The $\text{Pd}_{50}\text{Ni}_{50}$ is ~ 43 meV/atom above the convex hull, respectively. Upon possible stability of these phases due to entropic effects at higher temperatures would give rise to additional tie line with the NiO phase which are marked as red dashed line.

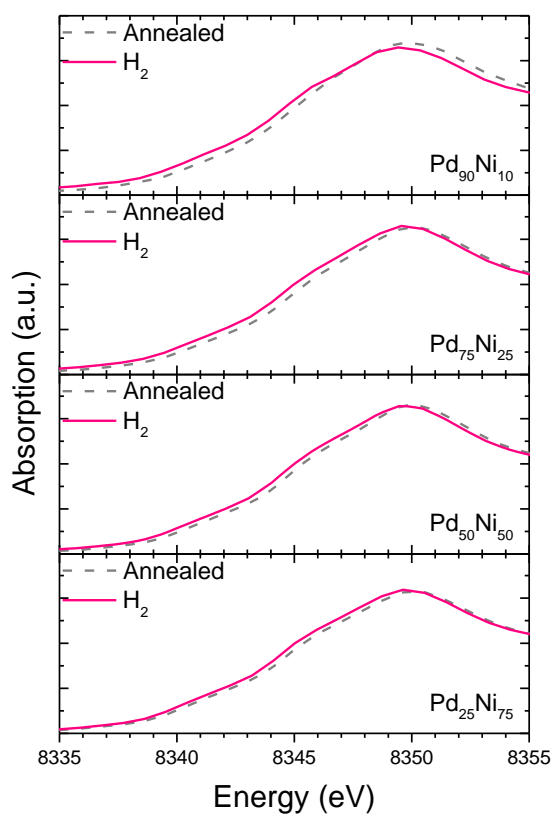


Figure S24: XANES measurements in the Ni K edge of the samples before and during H_2 exposure.

1. Pospelov, G. *et al.* *BornAgain*: software for simulating and fitting grazing-incidence small-angle scattering. *J. Appl. Crystallogr.* **53**, 262–276 (2020).
2. Yefanov, O. M. & Vartanyants, I. A. Three dimensional reconstruction of nanoislands from grazing-incidence small-angle X-ray scattering. *Eur. Phys. J. Spec. Top.* **167**, 81–86 (2009).
3. Grant, T. D. Ab initio electron density determination directly from solution scattering data. *Nat. Methods* **15**, 191–193 (2018).